Original Article

![CAMBRIDGE UNIVERSITY PRESS]

Late Neoarchaean tectonic environment in the Anshan-Benxi area: evidence of metamorphic supracrustal rocks

Guoyu Fan[1,2] , Xiaojie Dong[1,2] , Kai Zhu[3], Zhenghong Liu[1,2], Zhongyuan Xu[1,2] and Qingying Zhao[1,2]

[1]College of Earth Science, Jilin University, Changchun 130061, China; [2]Key Laboratory of Mineral Resources Evaluation in Northeast Asia, Ministry of Natural Resources, Changchun 130061, China and [3]Center for Lunar and Planetary Science, Institute of Geochemistry, Chinese Academy of Sciences, Guiyang 550081, China

Abstract

Zircon U-Pb geochronology, geochemistry and Hf isotope analysis of supracrustal rocks in the Anshan-Benxi area in the northeastern part of the North China Craton can help constrain their petrogenesis and tectonic background, providing evidence for a further investigation of the late Neoarchaean tectonic environment in the Anshan-Benxi area. The primary rock types observed among the supracrustal rocks in the Anshan-Benxi area comprise amphibolite, metamorphic rhyolite, metamorphic sandstone, chlorite schist, actinolite schist, among others. SHRIMP zircon U-Pb dating indicates that magmatic zircons from the amphibolite (GCN-1) formed at 2553 ± 18 Ma. Similarly, LA-ICP-MS zircon U-Pb dating reveals that magmatic zircons from the metamorphic rhyolite (G2304-1) were formed at 2457 ± 35 Ma. The peak age of the metamorphic sandstone is determined to be approximately 2500 Ma, suggesting that the supracrustal rocks in the Anshan-Benxi area originated in the late Neoarchaean. The protoliths of sericite quartz schist and metamorphic rhyolite are identified as rhyolitic volcanic rocks, displaying a right-leaning distribution pattern of rare earth elements (REEs). On the other hand, actinolite schist, chlorite schist and amphibolite are classified as basaltic volcanic rocks, exhibiting a flat REE pattern with a weak negative Eu anomaly. The $\varepsilon Hf(t)$ value of metamorphic rhyolite ranges between -1.19 and -1.47, with a two-stage depleted mantle model age of $tDM2(Ma) = 2922–3132$ Ma. The protolith magma of sericite quartz schist and metamorphic rhyolite originates from partial melting of 3.0 Ga basaltic crust, while the source of actinolite schist, chlorite schist and amphibolite are mainly derived from the mantle. In summary, the findings suggest that plate already existed in the late Neoarchaean or earlier, with magmatism in the Anshan-Benxi area likely occurring within an arc tectonic environment linked to plate subduction.

1. Introduction

The North China Craton (NCC), one of the oldest cratons on the Earth and the largest in China, contains rocks dating back to 3.8 Ga. Over time a series of tectonic, magmatic and metamorphic processes occurred. Recent geological investigations have delved into unravelling the Precambrian structure of the NCC, particularly elucidating a notable tectonothermal event that transpired during the Late Neoarchaean (2.55~2.50 Ga) (Bao *et al.*, 2020; Kusky, 2011; Li *et al.*, 2016; Wang *et al.*, 2018; Zhao *et al.*, 2005; Zhai, 2010, 2012; Zhao *et al.*, 2002). However, divergent perspectives exist regarding the cause of this event: some advocate for an island arc magmatism model within the framework of plate tectonics (Huang *et al.*, 2020; Kröner *et al.*, 2005; Wan *et al.*, 2010; Zhao *et al.*, 2000; Zhao *et al.*, 2005; Wan *et al.*, 2017), while others propose vertical tectonic mechanism such as mantle plume (Geng *et al.*, 2006; Wu *et al.*, 2021; Yu *et al.*, 2022; Zhao and Zhai, 2013; Zhai, 2010; Geng *et al.*, 2010). This ongoing debate centres on whether plate tectonics were active during the Neoarchaean, a fundamental question that has captivated researchers for decades.

Greenstone belts are extensively distributed worldwide. Currently, there are four predominant perspectives on the geodynamic origins of greenstone belt formation: (1) Mantle plume system, exemplified by the Onverwacht greenstone belt in the Barberton Craton (Stiegler *et al.*, 2008); (2) Island arc tectonic system, characterized by basic-intermediate-acidic volcanic rocks in greenstone belts, such as Limpopo greenstone belt in the Zimbabwe Craton (Khoza *et al.*, 2013); (3) Mantle plume-island arc tectonic system, where ultrabasic rocks and basic volcanic rocks like komatiite are common, as seen in greenstone belts like the Kolar greenstone belt in the Dharwar Craton (Balakrishnan *et al.*, 1991), Uchi greenstone belt (Hollings and Kerrich, 1999; Hollings *et al.*, 1999), Lumby Lake greenstone belt (Hollings and Kerrich, 1999; Hollings *et al.*, 1999), Abitibi belt greenstone belt (Kerrich *et al.*, 2008), Wawa greenstone belt (Polat *et al.*, 1999) and Kidd-MunroAbitibi greenstone belt (Wyman and

Kerrich, 2009; Wyman, 1999; Wyman et al., 2002) in the Superior Craton, Western Shandong Province granite-greenstone belt in the NCC (Wang, 2010); and (4) Mantle plume system of continental rift margin, characterized by bimodal volcanic rocks and the coexistence high-Mg and low-Mg basalts in greenstone belts like the Penakacherla greenstone belt (Manikyamba, 2004) and Sandur greenstone belt (Manikyamba et al., 2008) in the Dharwar Craton, Bulawayan greenstone belt in the Zimbabwe Craton (Prendergast, 2004) and Kalgoorlie greenstone belt in the Yilgarn Craton (Said et al., 2010). Numerous greenstone belts have been identified in the NCC (Guo et al., 2022, 2017; Lian et al., 2023; Li and Qian, 1995; Li et al., 2012; Wang, 2010; Zhu, 2016). Zhu (2016) categorized the greenstone belts of the eastern and central continental block orogenic belts of the NCC into two belts: the western and eastern greenstone belts, with a microcontinental belt between them. The western belt comprises western Liaoning, western Jilin, Northern Liaoning, eastern Hebei, Wutai and Dengfeng, while the eastern belt includes eastern Jilin (Jiapigou, Helong and Banshigou), Anshan, Jiaodong, Western Shandong and Lushan.

The formation of the upper greenstone belt in the NCC occurred in approximately four distinct stages: Middle Archaean (2.9~3.0 Ga); Early Neoarchaean (2.7~2.9 Ga); Late Neoarchaean (2.5~2.6 Ga) and Palaeoproterozoic, with the Neoarchaean (~2.7 Ga) representing the peak of greenstone belt formation (Wang, 2010). A typical greenstone belt consists of three layers: ultrabasic and basic volcanic rocks at the base, characterized by Komatiites; a central layer of calc-alkaline volcanic rock group, predominantly basalt, andesite, dacite and rhyolite, with chert; and sedimentary rocks at the top.

The Anshan-Benxi area, situated in the northeast of the NCC and north of the Jiao-Liao-Ji Palaeoproterozoic active belt, is distinguished by extensive Archaean geological bodies and widely spread Archaean greenstone belts. This region has been a focal point of geological research. Over the past three decades, numerous scholars have conducted detailed studies in the Anshan-Benxi area, leading to significant geological discoveries. However, unresolved controversies persist, particularly regarding the formation environment of the greenstone belt in this area. Presently, two main perspectives exist on this issue. One viewpoint suggests that the greenstone belt in the Anshan-Benxi area formed in an island arc environment with mantle material added: For instance, Dai et al. (2012) conducted a geochemical analysis on the surrounding rocks of the Chentaigou iron mines. By utilizing trace elements with stable geochemical properties, they were able to effectively determine the geotectonic environment of the rocks, concluding that the hidden greenstone belt in Chentaigou formed in an island arc environment (Dai et al., 2012). The other perspective posits that it formed in the back-arc basin. Wan (1992) collected an amphibolite from Gongchangling second mining area, systematically studying its petrography, petrochemistry and chronology and concluded that the greenstone belt originated in a tectonic environment of the back-arc marginal basin (Wan, 1992); Wang et al. (2013) conducted an extensive study on the geochemical characteristics of amphibolite and biotite granulite in Gongchangling mining area, concluding that Gongchangling greenstone belt was formed in the back-arc basin (Wang et al., 2013; Dai et al., 2013a) performed a geochemical analysis on the surrounding rocks of Waitoushan iron mines. They utilized trace elements with stable geochemical properties to effectively trace the geotectonic environment of the rocks, leading to the conclusion that the Waitoushan greenstone belt formed in the back-arc basin environment (Dai et al., 2013a,b); Guo et al. (2022)

examined the geochemistry and zircon U-Pb ages of tholeiites, calc-alkaline basalts, andesites, dacites and rhyolites in the Waitoushan-Gangchangling-Benxi area. Their analysis indicated that the lithological assemblages of basalts in the back-arc basin were erupted around 2.55~2.52 Ga, revealing that the Waitoushan-Gongchangling-Benxi area is positioned in the tectonic zone of the back-arc basin, with rocks in the tectonic belt experiencing consistent NE-SW compression during the back-arc closure (Guo et al., 2022); Tong et al. (2019) conducted in situ zircon U-Pb-Hf isotope, whole-rock geochemistry and Sm-Nd isotope analysis on the Dagushan metamorphic sedimentary rocks, suggesting that these sediments may have been deposited in the back-arc basin on the edge of an ancient continental crust (Tong et al., 2019). Recent studies on the chronology of greenstone belts have determined a formation age of approximately 2.5Ga, with some ancient greenstone remnants, such as ≥3.35 Ga supracrustal rocks in Chentaigou (Song et al., 1994).

The formation age of the greenstone belt in the Anshan-Benxi area is estimated to be around 2.55 Ga based on previous dating data. However, ongoing debates persist concerning the stratigraphic sequence, basement tectonic style, tectonic environment and origin of the abundant iron ore within the greenstone belt. As a result, this study aims to analyse the petrography, chronology and petrochemistry of the greenstone belt in the Anshan-Benxi area to contribute evidence towards comprehending the formation and evolution of the greenstone belt.

2. Regional geological setting

The Anshan-Benxi area, situated in the Jiao-Liao ancient land at the northeastern fringe of the NCC (Fig. 1a), serves as a significant iron ore resource reservoir in China, boasting a multitude of large and extra-large Banded iron formation (BIF) type iron deposit. The oldest geological formations in this region comprise the Anshan Group and its associated granite intrusions, constituting the Archaean basement. The granite covers approximately 70% of the area, while the supracrustal rocks encompass approximately 30%, with the granitic rocks primarily situated in Tiejiashan and Gongchangling. Overlaying the basement are several younger strata, including Palaeoproterozoic Liaohe Group; Neoproterozoic Qingbaikou and Nanhua systems; Palaeozoic Cambrian; Ordovician; Carboniferous; Permian; Mesozoic Triassic and Cenozoic Quaternary unconsolidated sediments. The region exhibits a two-layer structure comprising a crystalline basement and cover layer of the North China platform.

From the bottom up, the Anshan Group in the Anshan-Benxi area comprises the Cigou Formation, Dayugou Formation and Yingtaoyuan Formation. The Cigou Formation is predominantly distributed in locations such as Benxi Waitoushan, Maerling, Gongchangling and Sandaoling in Liaoyang. It consists of sericite chlorite schist, amphibolite, quartz hornblende schist, biotite quartz schist, magnetite quartzite, muscovite quartzite, among others. The Dayugou Formation is chiefly present in locations like Liaoyang Dayugou, Mianhuapuzi, Benxi East Dayugang and Sanjiazi. It is divided into two lithologic sequences: the initial part includes two-mica plagioclase gneiss, dolomitic plagioclase gneiss, biotite granite, two-mica sillimanite quartz schist, along with monzonitic granulite and biotite hornblende granulite. The latter segment comprises biotite leptite, biotite granulite, monzonite leptite, tourmaline-bearing leptite, mica schist, interspersed with amphibolite and magnetite quartzite. The Yingtaoyuan Formation is identified in locations like Anshan Yingtaoyuan, Hujiamiaozi,
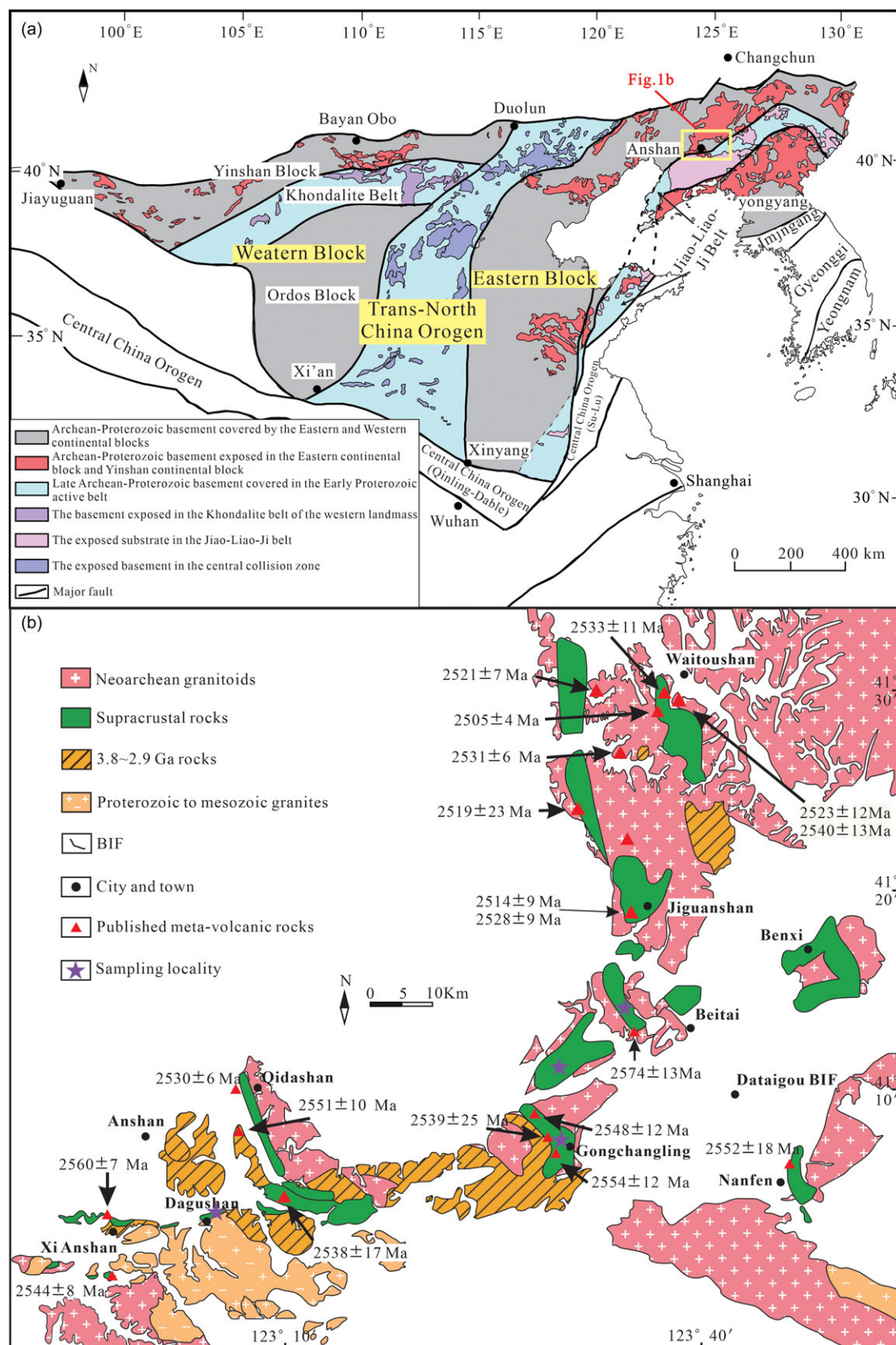
Figure 1. Geological map of North China Craton and the Anshan-Benxi area Modified from Guo *et al.* (2022). (a) Structural map of North China Craton; (b) Geological map of the Anshan-Benxi area and results of previous studies.
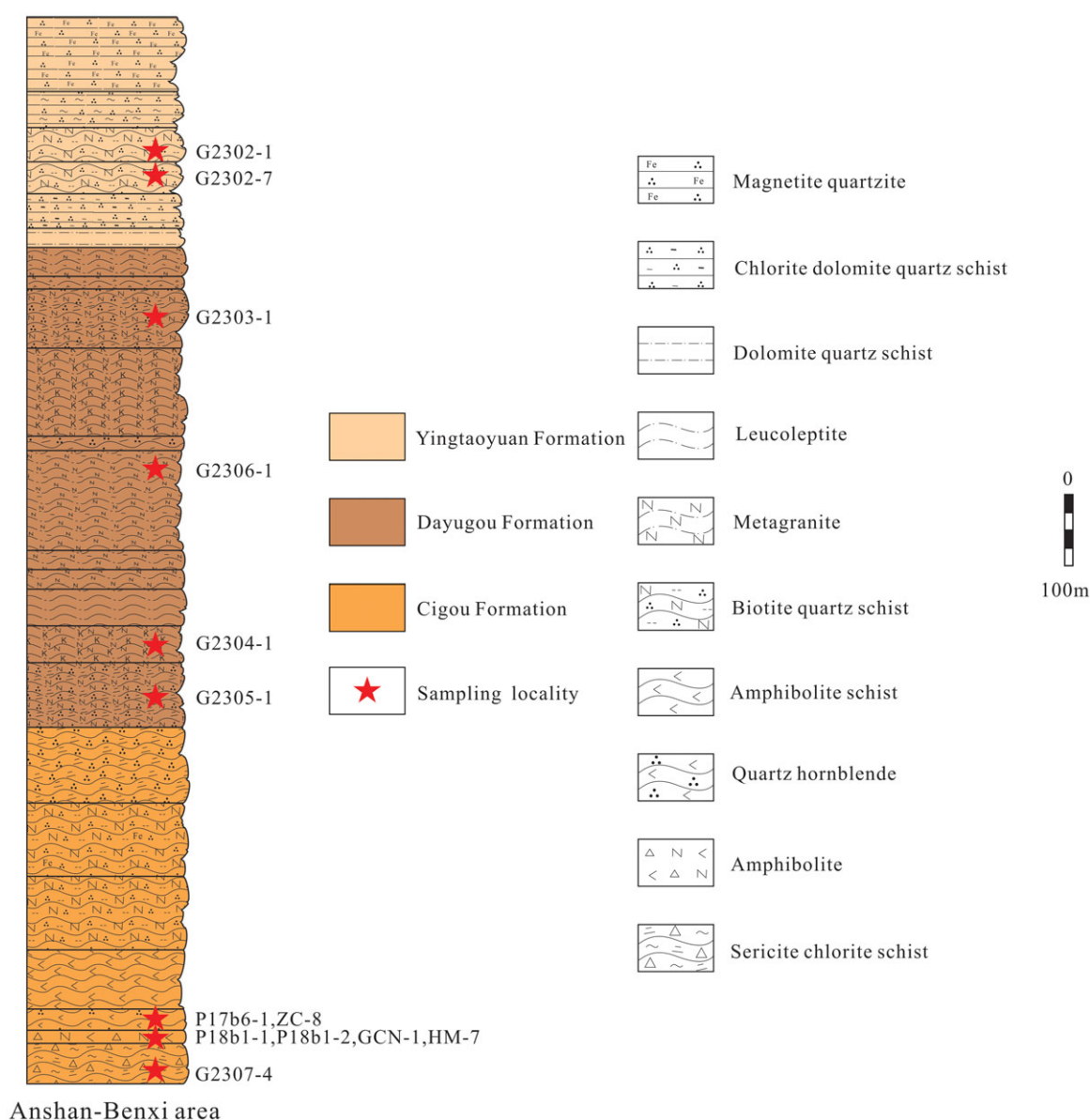
Figure 2. Column diagram of the Anshan group in the Anshan-Benxi area.

Yanqianshan, Dagushan, Donganshan and Xi'anshan, character-ized by sericulite chlorite schist, dolomite chlorite schist, chlorite schist, two-mica schist, phyllite and thick layers of magnetite quartzite. The stratigraphic lithologic features of the Anshan Group in the Anshan-Benxi area are illustrated in a column diagram (Fig. 2). Additionally, four fault structures are oriented in the NNE, NE, NW and EW directions.

The ancient continental nuclei in the Anshan-Benxi area originated between 3.8 and 3.0 Ga. Towards the end of the Late Archaean period, significant quantities of basic-medium-acidic magma erupted, forming the primary Archaean rocks in the Anshan-Benxi area, constituting the base of regional evolution. Subsequently, during the transition from the Late Archaean to the Early Proterozoic period, the basic magma underwent greenschist facies and amphibolite facies metamorphisms. Simultaneously, large-scale granitic magma emplaced upward to form rock masses such as the Qidashan granite and Gongchangling granite (Bao *et al.*, 2020; Li *et al.*, 2016; Wang *et al.*, 2016; Wang *et al.*, 2018;

Zhou *et al.*, 2008; Zhu, 2016). The Archaean crust in the Anshan-Benxi area underwent three significant tectonic deformation phases. The initial deformation phase occurred predominantly around 2.9 to 2.8 Ga, leading to the development of a dense and uniform gneiss in the Tiejiashan granite. This gneiss exhibits a NE-striking orientation with a steep dip angle, with predominant structural features observed in surface rocks including closed homoclinal folds and dense axial foliation. The subsequent stage of tectonic deformation was mainly formed at about 2.6 Ga (Dai *et al.*, 2013a, 2013b; Guo, 1994; Guo *et al.*, 2017; Liu *et al.*, 2017; Song *et al.*, 1996; Tong *et al.*, 2019; Wan *et al.*, 2007; Yang, 2013; Yin, 2006; Zhang *et al.*, 2013; Zhu *et al.*, 2015, 2016). Prior to this, Gongchangling granite invaded, making the surface rock become the xenolith of Gongchangling granite. Characterized by NNE and EW trending ductile shear belts, Zhu (2016) performed Muscovite Ar-Ar isotope dating on Donganshan granite situated in the vicinity of the ductile shear belt (Zhu, 2016), determining the formation age of muscovite to be 2545 ± 16 Ma, which coincides

Table 1. Sample information of Anshan-Benxi area

Sample	Lithology	Sampling location	Latitude, Longitude
GCN-1	Amphibolite	Dumushan mining area of Gongchangling	E:123°29′15″, N:41°7′24″
G2302-1	Sericite quartz schist	Jiajiagou	E:123°30′43.72″, N:41°11′42.75″
G2303-1	Meta-rhyolite	Jiajiagou	E:123°30′55.54″, N:41°11′49.54″
G2304-1	Meta-rhyolite	East of Qianpaifangcun, the south of Donggou	E:123°35′35.632″, N:41°12′40.201″
G2305-1	Meta-sandstone	South of Qianpaifangcun	E:123°35′8.293″, N41°12′19.85″
G2306-1	Meta-sandstone	Donggou	E:123°35′35.632″, N:41°12′40.201″
G2307-1	Chlorite schist	Hujiamiaozi	E:123°8′13.91″, N:41°6′48.59″
P17b6-1	Actinolite schist	Gongchangling	
ZC-8	Actinolite schist	Gongchangling	
P18b1	Amphibolite	Gongchangling	
HM-7	Amphibolite	Hujiamiaozi	

with the thermal disturbance period of deformation and metamorphism events on Donganshan granite. The third tectonic deformation phase, occurring around 2.0 Ga, led to the transformation of the NNW ductile shear belt of nappe into a strike-slip ductile shear belt and the EW-slip ductile shear belt into a nappe ductile shear belt, resulting in the formation of structural schist (Guo, 1994). The intricate tectonic deformation history caused the supracrustal rocks in the Anshan-Benxi area to undergo complex internal deformation. Liu (2019) categorized the formation and evolution process of the granite-greenstone belt base in the Anshan-Benxi area into two primary stages: the initial BIF iron deposit phase and the emplacement of Qidashan granite in the Late Neoarchaean period. The accompanying metamorphic deformation distorted the original Archaean tectonic configuration and the distribution characteristics of the original iron-bearing structures (Liu *et al.*, 2017).

3. Sample collection and Petrology

This study focuses on actinolite schist, sericite quartz schist, chlorite schist, meta-rhyolite, meta-sandstone and amphibolite from the Anshan-Benxi area. The primary objective is to investigate their petrology, whole-rock geochemistry, zircon U–Pb and Lu–Hf isotopes. The sampling locations are illustrated in Fig. 1b, Fig. 2, Table 1.

Actinolite schist, sourced from the Yingtaoyuan Formation of the Anshan Group, displays a yellow-green weathered surface and a grey-green fresh surface with well-developed slaty cleavage. It exhibits a cylindrical granoblastic structure and schistose structure (Fig. 3a). Actinolite schist is primarily composed of quartz (45%), actinolite (35%), garnet (10%) and hornblende (10%) (Fig. 3b).

Sericite quartz schist, obtained from the Yingtaoyuan Formation of the Anshan Group, displays a soil-yellow weathered surface and a greyish-brown fresh surface with a lepido granoblastic texture and schistose structure. Sericite quartz schist is composed of sericite (10%), biotite (5%), plagioclase (15%), microcline (10%), quartz (60%) and a small amount of garnet (2%). Sericitization occurs in plagioclase, and microcline has a grid twin (Fig. 3c).

Meta-rhyolite, sourced from the Dayugou Formation of the Anshan Group, displays a yellowish-brown weathered surface and a greyish-white fresh surface with porphyritic texture and massive structure. It comprises matrix and porphyry. The porphyry is

composed of quartz. The matrix is cryptocrystalline, consisting of microcrystalline perthite, mica, etc., displaying a flow structure. The observation of an augen structure indicates ductile deformation in this rock (Fig. 3d). Meta-rhyolite is composed of quartz (40%), feldspar (10%), sericite (28%), muscovite (10%), biotite (10%) and actinolite (2%). Muscovite is rose-red under single polarizing lens, containing Li, with actinolite acicular (Fig. 3e).

Meta-sandstone, extracted from the Dayugou Formation of the Anshan Group, exhibits a rust-brown weathered surface and earthy yellow fresh surface with a lepido granoblastic texture and schistose structure. It is composed of feldspar (48%), quartz (30%), biotite (20%) and muscovite (2%). The minerals exhibit a rounded shape with fine grain size, and sericitization occurs in plagioclase (Fig. 3f).

Chlorite schist, taken from the Cigou Formation of the Anshan Group, is yellowish-green on weathered surface and grey-green on fresh surface, displaying a lepido granoblastic texture and schistose structure. It consists of chlorite (70%) and quartz (30%). Chlorite displays abnormal interference colours such as indigo and rust, and it is both orientated and continuous (Fig. 3g).

Amphibolite, also from the Cigou Formation of the Anshan Group, is greyish-brown in weathering and greyish green on fresh surface, with a cylindrical granoblastic structure and massive structure. Amphibolite is composed of hornblende (60%), plagioclase (30%) and biotite (10%). Most of the hornblende is actinized, with plagioclase showing sericitized (Fig. 3h).

4 Analysis methods

4.a. Zircon U-Pb isotope dating

Zircon separation was completed at Langfang Keda Rock and Mineral Sorting Technology Service Co., Ltd. Zircon mount and image acquisition (including transmitted light, reflected light and cathode luminescence) were completed in Beijing Zirconia Linghang Technology Co., Ltd. Zircon U-Pb dating of samples G2303-1, G2304-1, G2305-1 and G2306-1 was completed by LA-ICP-MS analysis at the Key Laboratory of Mineral Resources Evaluation in Northeast Asia, Ministry of Natural Resources, Jilin University, China. The laser denudation system is a GeoLasPro 193nmArF excimer laser produced by COMPEx GMBH in Germany. The sample was analysed using a 32μm diameter laser
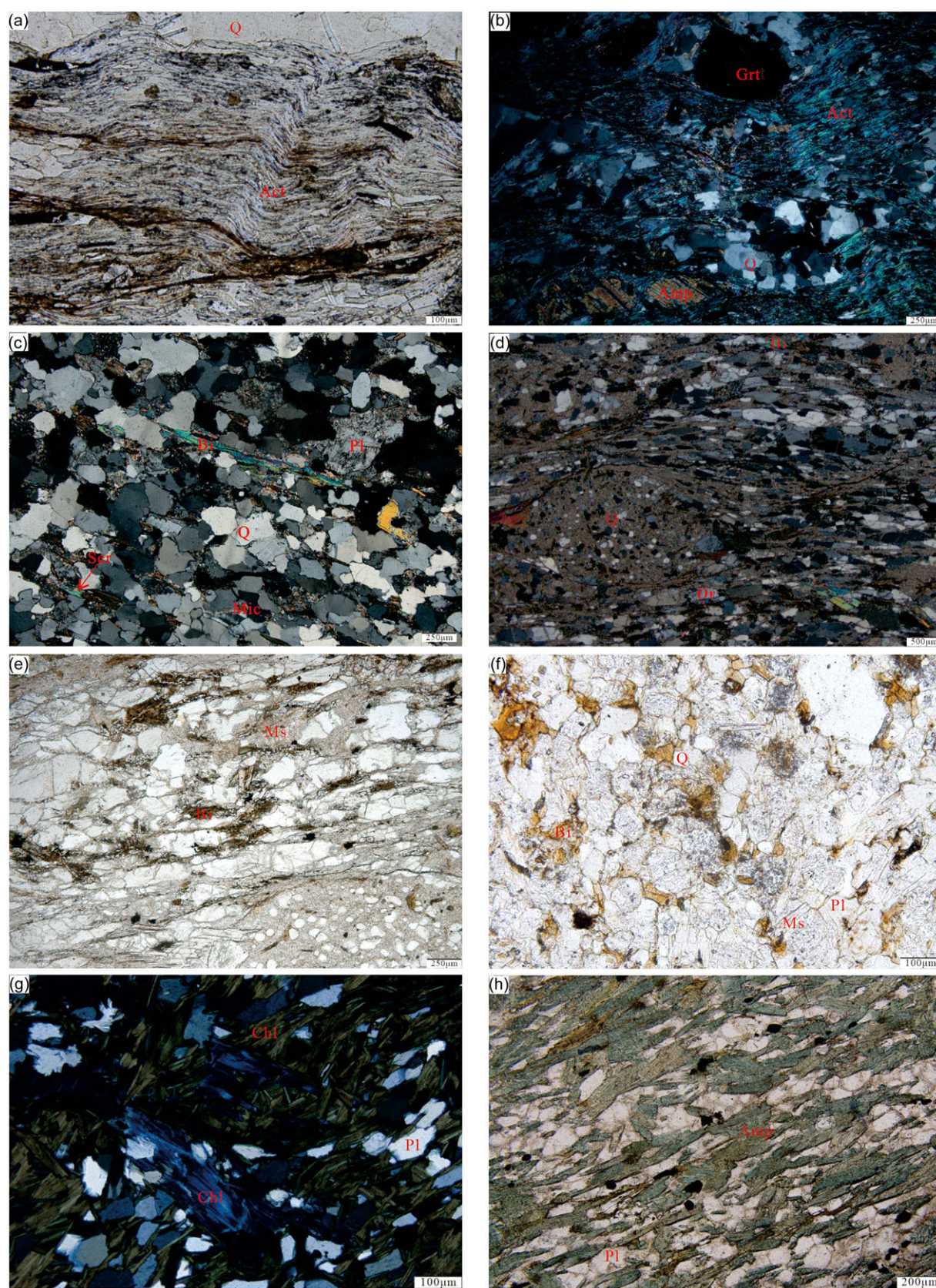
Figure 3. Photographs of supracrustal rocks of the Anshan Group in the Anshan-Benxi area. (a) Slaty cleavage in actinolite schist; (b) Actinolite schist; (c) Sericite quartz schist; (d) Augen structure in meta-rhyolite; (e) Meta-rhyolite; (f) Meta-sandstone; (g) Chlorite schist; (h) Amphibolite. Act-Actinolite, Amp-Amphibole, Bi-Biotite, Chl-Chlorite, Grt-Garnet, Mic-Microcline, Ms-Muscovite, Or-Orthoclase, Pl-Plagioclase, Q-Quartz, Ser-Sericite.

beam with a frequency of 7Hz. The Agilent7900 type ICP-MS instrument is used in conjunction with the laser, and He is used as the carrier gas of the denudating material (Eggins *et al.*, 1998; Jackson *et al.*, 2004). The instrument optimization adopts the standard reference material NIST610 of synthetic silicate glass developed by the National Institute of Standards and Technology of the United States. In situ U-Pb analysis of zircon was carried out by using the 91500 standard zircon external correction method, please refer to Yuan *et al.* (2004) for the specific experimental test process. Isotope ratios and ages of ^{207}Pb/^{206}Pb、^{206}Pb/^{238}U and ^{207}Pb/^{235}U were calculated using Glitter software (Liu *et al.*, 2010). The method of Andersen (2002) was used to correct the results by ordinary lead, and the Isoplot programme was used to calculate the age. The error for a single data is 1σ and the weighted mean age error is 95% confidence. The ^{207}Pb/^{206}Pb age is used as the zircon age.

Zircon U-Pb dating of sample GCN-1 was analysed by SHRIMP II ion probe in Beijing SHRIMP Center. The dating principles and methods are described in Mckibben *et al.* (1998), and the dating process is detailed in Song *et al.* (2002) and Wan *et al.* (2005). The primary ion flow O2 intensity is 4.5nA, and the beam spot size is ~30μm. Standard zircon TEM and M257 are used for ^{206}Pb/^{238}U age and U and Th content calibration, respectively. The ratio of standard zircon (TEM) to the sample to be tested is 1:4, and each data point consists of 5 sets of scans, SHRIMP data are calculated by SQUID programme based on ^{204}Pb contents subtracting common lead, ISOPLOT programme calculates the weighted average value and draws U-Pb concordia plot (Vermeesch, 2018). The individual data error is 1σ, and the weighted mean age error is 95% confidence.

4.b. In situ analysis of Hf isotopic composition

The Hf isotope analysis of zircon was carried out by LA-MC-ICP-MS in Wuhan Sample Solution Analytical Technology Co., Ltd. Experiments of in situ Hf isotope ratio analysis were conducted using a Neptune Plus MC-ICP-MS (Thermo Fisher Scientific, Germany) in combination with a Geolas HD excimer ArF laser ablation system (Coherent, Göttingen, Germany) that was hosted at the Wuhan Sample Solution Analytical Technology Co., Ltd, Hubei, China. A 'wire' signal smoothing device is included in this laser ablation system, by which smooth signals are produced even at very low laser repetition rates down to 1 Hz (Hu *et al.*, 2015). Helium was used as the carrier gas within the ablation cell and was merged with argon (makeup gas) after the ablation cell. Small amounts of nitrogen were added to the argon makeup gas flow for the improvement of sensitivity of Hf isotopes (Hu et al. 2012). All data were acquired on zircon in single spot ablation mode at a spot size of 44 μm or 32 μm. Analytical methods are the same as described by Hu et al. (2012). The new high-performance cone combination designed by Neptune Plus was used in the analysis. The Hf isotope standard calibration of zircon was used with 91500, GJ-1 international zircon and SP-1 zircon to better monitor the quality of the measured isotope data. The external precision (2SD) of 91500 and GJ-1 is better than 0.000020 (Zhang *et al.*, 2020).

4.c. Major and trace elements

The analysis of major elements and trace elements was carried out in Aoshi Analytical Testing (Guangzhou) Co., Ltd. After cleaning, grinding and crushing the fresh samples removed from the weathered surface, 200 mesh rock powder was obtained for the analysis of major and trace elements. The major elements were determined by X-ray fluorescence spectrometry (ME-XRF26d).

The relative error of precision of ME-XRF26d method was controlled at <5 %, with the relative error of accuracy being controlled at < 5 %. Trace elements and rare earth elements were determined by inductively coupled plasma mass spectrometer using ICP-MS (ME-MS81). The relative error of precision of ME-MS81 method was controlled at < 10 %, with the relative error of accuracy being controlled at < 10 %.

5 Results

5.a. Zircon U–Pb dating

The zircons of amphibolite (GCN-1) are predominantly granular characteristics with an aspect-to-width ratio of approximately 1:1 and an average particle size of about 100μm. Zircons are mostly broken, the shape is not complete, along with many cracks on the surface. Zircons develop zoning, mainly broad zoning, with a small amount of zircons developing fine zoning. Some zircons display distinct bright metamorphic edges (Fig. 4). A total of 19 zircon grains were analysed in this sample, the data are listed in Table 2. Th contents of the zircon sample range from 79.78ppm to 1155.91ppm, while U contents range from 30.61ppm to 568.73ppm. The Th/U values vary from 0.51 to 23.58, with only one zircon exhibiting a value of 23.58, characteristic of magmatic zircons. The apparent age of the zircons falls within the range of 2577 Ma to 2543 Ma. On the zircon U-Pb age concordia diagram, some data points align with the ^{206}Pb/^{238}U-^{207}Pb/^{235}U concordia curve. The ^{207}Pb/^{206}Pb weighted average age of 11 data points (1.1,2.1,3.1,6.1,7.1,9.1,11.1,11.1,13.1,14.1,15.1,16.1) is 2571 ± 5.3Ma (MSWD = 1.5), interpreted as the formation age of the protolith of amphibolite. (Fig. 5a).

The zircons from meta-rhyolite (G2304-1) exhibit cylindrical or equiaxed shapes. They are more idiomorphic with good crystal shape, with uniform size averaging around 100 μm. The length-width ratio falls between 1:2 and 1:3. In cathodoluminescence diagrams, most zircons exhibit irregular rhythmic bands with rings, suggesting recrystallization at varying ages. Metamorphic accretion edges on zircons are minimal (Fig. 4). A total of 30 zircon grains were analysed, all falling within the magmatic zircon compositional domain. Data for these zircons are detailed in Table 2. Results reveal Th contents ranging from 20.34 ppm to 367.07 ppm, U contents ranging from 62.78 ppm to 395.22 ppm. The Th/U value ranges from 0.25 to 1.35, with only two values below 0.4, indicative of magmatic zircon. The apparent ages of these zircons cluster around 2552 Ma to 2450 Ma. On the zircon U-Pb age concordia diagram, some data points lie on the ^{206}Pb/^{238}U-^{207}Pb/^{235}U concordia line (Fig. 5b). Points below the concordia curve form a discordant line with an upper intercept age of 2500 ± 40 Ma (MSWD=4.4). The ^{207}Pb/^{206}Pb weighted mean age of 16 data points (G2304-2-1, G2304-2-3, G2304-2-4, G2304-2-5, G2304-2-9, G2304-2-12, G2304-2-13, G2304-2-15, G2304-2-17, G2304-2-22, G2304-2-23, G2304-2-24, G2304-2-26, G2304-2-27, G2304-2-28, G2304-2-29) is 2470 ± 20 Ma (MSWD = 4.6). LA-ICP-MS zircon U-Pb dating was unfeasible due to the narrow or absent metamorphic accretionary margin in this sample.

The zircons of meta-sandstone (G2305-1) exhibit signs of degradation, damaging into the form of residual columns, fragments and subcircular shapes. These characteristics suggest weathering and transportation over a considerable distance, displaying typical detrital zircon features. Zircons grain sizes range from 50 μm to 150 μm, with an aspect ratio between 1:1 and 1:3. In the cathodoluminescence diagrams, most zircons develop

Figure 4. CL image of representative zircon (The red solid circle is the U-Pb spot, and the yellow dotted circle is the Lu-Hf isotope spot.).

annular bands and plate-like strips, indicating recrystallization at different times. Metamorphic and accretionary rims on these zircons are generally absent (Fig. 4). A total of 80 zircon grains were analysed, and the data are listed in Table 2. Th contents of zircon in this sample range from 54.05 ppm to 904.36ppm, U contents ranged from 89.53ppm to 1058.2ppm, with the value of Th/U ranging from 0.12 to 1.33. The majority of the zircon grains have Th/U ratios exceeding 0.4, and CL images reveal well-defined oscillatory ring structures, indicating magmatic origin. Validated data yielded zircon ages ranging from 2172 Ma to 2980 Ma (Fig. 5c), with a prominent peak at 2500 Ma (Fig. 5d).

The meta-sandstone (G2306-1) contains intact zircon crystals, predominantly cylindrical in shape, with rounded zircon grains ranging from 75 μm to 150 μm in size and aspect ratios between 1:1 and 1:3. Cathodoluminescence diagrams indicate that most zircons exhibit ring bands, suggesting multiple recrystallization events with narrow metamorphic accretion margins (Fig. 4). A total of 80 zircon grains were analysed, and the results are presented in Table 2. Th contents of zircon grains ranged from 15.18 ppm to 2756.36 ppm, while U contents varied from 79.47 ppm to 1421.02 ppm. The Th/U values range from 0.06 to 2.32, respectively. The majority of zircons have Th/U ratios above 0.4, displaying well-defined oscillatory ring structure in CL images, indicating a magmatic origin. The range of ages obtained from valid data varies from 1970 Ma to 3099 Ma (Fig. 5e), with a prominent peak at 2500 Ma (Fig. 5f).

5.b. Zircon Hf isotopic data

The study presents the results of in situ Hf isotope analysis for one sample (G2304-1) of zircon, as shown in Table 3. The $^{176}Hf/^{177}Hf$ radios of 10 zircons from meta-rhyolite (G2304-1) range from 0.281175 to 0.281306, with corresponding $\varepsilon_{Hf}(t)$ values ranging from -1.19 to 1.47. The calculated Hf model age, expressed as t_{DM2} (Ma), falls within the range of 2922 Ma to 3132 Ma. The zircon age-$\varepsilon_{Hf}(t)$ diagram for meta-rhyolite in the Anshan-Benxi area is depicted in Fig. 6, along with the detailed results of zircon Hf isotope analysis detailed in Table 3.

5.c. Geochemistry

Sericite quartz schist: SiO_2 contents range from 77.82 to 78.89wt.%, indicative of acidic rock. The Al_2O_3 contents range from 20.94 to 22.72wt.%; CaO contents from 0.66 to 0.71wt.%, Fe_2O_{3T} contents from 1.80 to 1.84wt.%, total alkali Na_2O+K_2O contents from 5.56 to 5.85wt.%, with minimal amounts of other oxides. The loss on ignition (LOI) ranges from 1.24 to 1.36wt.%, $Mg^\#$ from 30.71 to 32.37, Rittmann Index (σ) from 0.86 to 0.98 (Table 4), indicating that the samples are mainly calc-alkaline rocks, as depicted in the diagram (Fig. 8f, h, i). In the TAS (Na_2O+K_2O vs. SiO_2) and SiO_2 vs. Zr/TiO_2 diagrams, sericite quartz schist falls within the rhyolite region (Fig. 8d, e). Based on the comparison of Al_2O_3, Na_2O+K_2O and Na_2O+K_2O+CaO contents, the rock is classified as peraluminous, further affirmed by its position in the ANK-ACNK diagram within the peraluminous region (Fig. 8a).

Table 2. Analysis results of Zircon U-Pb isotope

spot	[U] ppm	[Th] ppm	[^{206}Pb] ppm	Th/U	^{207}Pb/^{235}U	± δ%	^{206}Pb/^{238}U	± δ%	^{207}Pb/^{206}Pb	± δ%	^{207}Pb/^{206}Pb age(Ma)	± δ	^{206}Pb/^{238}U age(Ma)	± δ
G2304-1														
G2304-1-1	211.57	154.69	449.83	0.73115	9.97395	0.21663	0.45974	0.01057	0.15816	0.00307	2436	17	2438	47
G2304-1-2	319.78	259.37	485.13	0.81109	6.73725	0.14461	0.32369	0.0074	0.1517	0.0029	2365	17	1808	36
G2304-1-3	103.5	110.84	255.64	1.07092	9.93329	0.23562	0.4634	0.01092	0.15619	0.00342	2415	18	2455	48
G2304-1-4	202.05	155.04	416.5	0.76734	9.72266	0.21017	0.45308	0.01034	0.15632	0.00303	2416	17	2409	46
G2304-1-5	174.14	114.06	324.96	0.65499	9.93102	0.21912	0.45764	0.0105	0.15804	0.00315	2435	18	2429	46
G2304-1-6	275.95	206.94	468.75	0.74992	7.46447	0.16007	0.35221	0.00797	0.15427	0.00297	2394	17	1945	38
G2304-1-7	216.41	203.4	399.05	0.93988	8.68893	0.1871	0.39733	0.00899	0.15915	0.00309	2447	17	2157	41
G2304-1-8	62.78	20.34	168.58	0.32399	12.50473	0.2925	0.50808	0.01186	0.17908	0.00388	2644	18	2648	51
G2304-1-9	159.14	120.94	387.42	0.75996	10.26343	0.22653	0.46818	0.01064	0.15947	0.00321	2450	17	2476	47
G2304-1-10	395.22	367.07	583.5	0.92877	6.76029	0.14521	0.31568	0.0071	0.15575	0.00303	2410	17	1769	35
G2304-1-11	307.14	313.14	399.28	1.01954	6.55964	0.14128	0.30517	0.00684	0.15627	0.00306	2416	17	1717	34
G2304-1-12	139.72	98.86	343.42	0.70756	10.53138	0.2424	0.47608	0.0109	0.1608	0.00343	2464	18	2510	48
G2304-1-13	191.94	158.38	431.25	0.82515	10.41324	0.2238	0.47074	0.01051	0.16077	0.00315	2464	17	2487	46
G2304-1-14	341.34	334.24	468.11	0.9792	6.59128	0.14123	0.30275	0.00674	0.1582	0.00309	2437	17	1705	33
G2304-1-15	138.42	187.57	285.82	1.35508	10.42568	0.22897	0.46759	0.01048	0.16199	0.00327	2477	17	2473	46
G2304-1-16	215.3	156.15	392.12	0.72527	9.07084	0.19603	0.38888	0.00864	0.16941	0.00336	2552	17	2118	40
G2304-1-17	182.87	114.5	392.82	0.62613	10.21539	0.22403	0.46221	0.01029	0.16049	0.00325	2461	17	2449	45
G2304-1-18	116.62	76.62	286.09	0.65701	12.34156	0.28792	0.50619	0.01154	0.17702	0.00388	2625	18	2640	49
G2304-1-19	300.13	278.44	409.96	0.92773	6.60355	0.14179	0.30905	0.0068	0.15512	0.00307	2403	17	1736	33
G2304-1-20	218.89	241.66	367.59	1.10403	6.40302	0.14209	0.36004	0.00793	0.12909	0.00266	2086	18	1982	38
G2304-1-21	283.1	274.81	437.33	0.97072	7.40169	0.15857	0.32792	0.00717	0.16378	0.00326	2495	17	1828	35
G2304-1-22	107.53	83.22	247.01	0.77392	11.23004	0.26709	0.485	0.011	0.16799	0.0038	2538	18	2549	48
G2304-1-23	207.71	168.65	457.33	0.81195	10.98648	0.23731	0.47344	0.01034	0.16835	0.00339	2541	17	2499	45
G2304-1-24	126.83	97.98	286.9	0.77253	10.66894	0.23182	0.47403	0.01036	0.16326	0.00332	2490	17	2501	45
G2304-1-25	368.41	92.54	608.85	0.25119	8.22463	0.19894	0.3567	0.0078	0.16723	0.00545	2530	56	1967	37
G2304-1-26	113.42	84.8	276.8	0.74766	10.31865	0.23538	0.46571	0.01028	0.16068	0.00348	2463	17	2465	45
G2304-1-27	175.13	133.81	395.4	0.76406	10.54007	0.22721	0.469	0.01014	0.16297	0.0033	2487	17	2479	44
G2304-1-28	197.73	108.64	419.34	0.54944	10.37059	0.2262	0.46521	0.01009	0.16164	0.00333	2473	17	2463	44
G2304-1-29	128.32	89.89	283.14	0.70051	10.85075	0.24082	0.47643	0.01038	0.16513	0.00348	2509	17	2512	45
G2304-1-30	254.44	152.22	400.52	0.59826	6.71078	0.23111	0.33378	0.00772	0.14582	0.00605	2297	73	1857	37

(Continued)

Table 2. (*Continued*)

spot	[U] ppm	[Th] ppm	[206Pb] ppm	Th/U	207Pb/235U	± δ%	206Pb/238U	± δ%	207Pb/206Pb	± δ%	207Pb/206Pb age(Ma)	± δ	206Pb/238U age(Ma)	± δ
G2305-1														
G2305-1-1	326.75	82.43	355.38	0.25253	7.34896	0.21444	0.31387	0.00754	0.16982	0.00642	2556	65	2155	26
G2305-1-2	250.7	307.92	377.39	1.23457	7.1198	0.17293	0.31194	0.00731	0.16438	0.00346	2501	18	2127	22
G2305-1-3	832.41	904.36	547.98	1.08696	3.44771	0.08269	0.13816	0.00322	0.17975	0.00373	2651	18	1515	19
G2305-1-4	1058.2	725.27	617.21	0.68493	2.61109	0.11806	0.12769	0.00336	0.14831	0.00776	2327	92	1304	33
G2305-1-5	143.47	87.28	317.61	0.60976	11.46335	0.27747	0.4872	0.0114	0.16954	0.00357	2553	18	2562	23
G2305-1-6	254.47	135.47	532.62	0.53191	11.25525	0.26778	0.46237	0.01074	0.17546	0.00361	2610	18	2545	22
G2305-1-7	158.05	68.11	306.09	0.43103	9.38748	0.30484	0.40825	0.01004	0.16677	0.00679	2526	70	2377	30
G2305-1-8	308.3	191.47	542.53	0.62112	9.20964	0.21976	0.38856	0.00902	0.17089	0.00355	2566	18	2359	22
G2305-1-9	390.05	261.12	557.82	0.67114	7.80778	0.18452	0.32486	0.00752	0.17332	0.00355	2590	18	2209	21
G2305-1-10	350.05	331.35	479.29	0.9434	6.79327	0.16227	0.28931	0.00671	0.16935	0.00353	2551	18	2085	21
G2305-1-11	329.69	243.46	475.49	0.74074	7.05784	0.16674	0.30581	0.00706	0.16651	0.00343	2523	18	2119	21
G2305-1-12	243.52	103.36	540.51	0.42373	11.23237	0.26502	0.48217	0.01113	0.16809	0.00346	2539	18	2543	22
G2305-1-13	218.38	93.93	439.4	0.43103	10.22536	0.24147	0.44002	0.01015	0.16771	0.00346	2535	18	2455	22
G2305-1-14	264.5	161.05	577.97	0.60976	11.06891	0.26075	0.47955	0.01105	0.1666	0.00343	2524	18	2529	22
G2305-1-15	573.68	345.42	664.24	0.60241	5.64676	0.1907	0.25669	0.00629	0.15955	0.00666	2451	72	1923	29
G2305-1-16	184.9	129.17	386.81	0.6993	10.63439	0.2503	0.44834	0.01031	0.17128	0.00354	2570	18	2492	22
G2305-1-17	229.12	142.71	544.43	0.62112	11.88486	0.28313	0.49471	0.01143	0.1735	0.00366	2592	18	2595	22
G2305-1-18	336.95	262.67	542.05	0.78125	7.05017	0.33396	0.30545	0.00821	0.1674	0.00912	2532	94	2118	42
G2305-1-19	91.74	60.26	196.52	0.65789	11.86819	0.2919	0.49229	0.01151	0.17416	0.00385	2598	18	2594	23
G2305-1-20	753.12	345.83	519.33	0.45872	2.42086	0.11038	0.12943	0.00331	0.13565	0.00709	2172	93	1249	33
G2305-1-21	439.81	295.61	560	0.67114	6.29501	0.20942	0.27598	0.00672	0.16543	0.00682	2512	71	2018	29
G2305-1-22	284.31	304.75	410.23	1.07527	7.05122	0.16419	0.30313	0.00691	0.16817	0.00348	2540	18	2118	21
G2305-1-23	503.28	239.4	615.34	0.47619	5.6156	0.16765	0.26633	0.00627	0.15292	0.00581	2379	66	1918	26
G2305-1-24	326.95	254.42	466.05	0.77519	7.44222	0.17223	0.3125	0.00711	0.17222	0.00354	2579	18	2166	21
G2305-1-25	564.07	71.5	581.49	0.12674	4.54801	0.11154	0.21078	0.00475	0.15649	0.00521	2418	58	1740	20
G2305-1-26	408.92	219.88	625.51	0.53763	7.76036	0.1783	0.3386	0.00767	0.1658	0.00339	2516	18	2204	21
G2305-1-27	844.81	472.9	731.27	0.55866	3.66918	0.1358	0.18176	0.00445	0.14641	0.0065	2304	78	1565	30
G2305-1-28	312.04	194.24	549.11	0.62112	8.57155	0.30512	0.36608	0.00903	0.16982	0.00736	2556	74	2294	32
G2305-1-29	186.8	156.76	403.82	0.84034	11.04384	0.25516	0.4785	0.01085	0.16704	0.00345	2528	18	2527	22

(*Continued*)

Table 2. (*Continued*)

G2305-1-30	258.35	251.42	449.8	0.97087	9.21334	0.21152	0.38899	0.0088	0.17144	0.00352	2572	17	2359	21
G2305-1-31	212.78	177.01	398.93	0.83333	9.02208	0.207	0.39562	0.00893	0.16511	0.0034	2509	18	2340	21
G2305-1-32	300.81	187.06	566.6	0.62112	9.60113	0.29992	0.41332	0.00985	0.16848	0.00662	2543	67	2397	29
G2305-1-33	558.53	744.31	575.37	1.33333	6.12876	0.13921	0.24971	0.00561	0.17775	0.00362	2632	17	1994	20
G2305-1-34	201.28	176.33	353.3	0.87719	9.06494	0.20798	0.39145	0.00882	0.16773	0.00347	2535	17	2345	21
G2305-1-35	296.55	255.44	508.08	0.86207	8.61967	0.1958	0.37293	0.00837	0.16744	0.00342	2532	17	2299	21
G2305-1-36	122.54	117.76	273.95	0.96154	11.02579	0.25553	0.47934	0.01083	0.16667	0.00351	2524	18	2525	22
G2305-1-37	98.92	55.38	257.95	0.55866	11.11008	0.28279	0.47963	0.01123	0.16786	0.00399	2536	19	2532	24
G2305-1-38	764.04	715.17	648.52	0.93458	4.19547	0.15738	0.18588	0.0046	0.1637	0.00736	2494	78	1673	31
G2305-1-39	288.39	166.24	571.32	0.57803	9.44628	0.21262	0.41573	0.00928	0.16471	0.00335	2505	17	2382	21
G2305-1-40	224.79	86.4	488.6	0.38462	11.48128	0.26308	0.48754	0.01095	0.17072	0.00356	2565	17	2563	21
G2305-1-41	331.79	207.16	646.07	0.625	9.40172	0.21069	0.40904	0.0091	0.16669	0.00339	2525	17	2378	21
G2305-1-42	122.42	119.14	270.14	0.97087	10.41761	0.42035	0.4412	0.01121	0.17125	0.00817	2570	82	2473	37
G2305-1-43	528.83	303.89	649.38	0.57471	5.62131	0.17385	0.26091	0.0061	0.15626	0.00606	2416	67	1919	27
G2305-1-44	425.11	263.72	607.06	0.62112	6.87446	0.22454	0.30125	0.00716	0.16551	0.00669	2513	70	2095	29
G2305-1-45	550.91	298.75	675.81	0.54348	5.92611	0.1784	0.27181	0.00631	0.15813	0.00601	2436	66	1965	26
G2305-1-46	213.17	183.64	361.48	0.86207	8.09295	0.32147	0.36125	0.00902	0.16248	0.00762	2482	81	2241	36
G2305-1-47	593.23	417.61	703.85	0.70423	5.26931	0.11709	0.25827	0.0057	0.14809	0.00301	2324	17	1864	19
G2305-1-48	116.98	99.62	263.29	0.8547	11.14101	0.2552	0.48198	0.01077	0.16779	0.00355	2536	17	2535	21
G2305-1-49	567.96	508.54	575.56	0.89286	4.66412	0.10349	0.21718	0.00479	0.15591	0.00317	2412	17	1761	19
G2305-1-50	315.74	195.53	477.98	0.62112	7.46925	0.16584	0.3358	0.00741	0.1615	0.00329	2471	17	2169	20
G2305-1-51	492.92	251.1	670.32	0.5102	6.03505	0.17704	0.2854	0.00653	0.15336	0.00571	2384	65	1981	26
G2305-1-52	323.42	362.16	660.95	1.1236	10.67879	0.23529	0.44294	0.00974	0.17511	0.00355	2607	17	2496	20
G2305-1-53	253.55	176.37	524.6	0.69444	10.97124	0.24664	0.47884	0.0106	0.16643	0.00346	2522	17	2521	21
G2305-1-54	587.64	290.85	633.33	0.49505	4.85384	0.14533	0.22815	0.00524	0.1543	0.00582	2394	66	1794	25
G2305-1-55	366.14	188.83	604.43	0.51546	7.96738	0.23102	0.35839	0.00821	0.16124	0.00596	2469	64	2227	26
G2305-1-56	421.68	228.19	563.23	0.54054	6.39499	0.14021	0.28825	0.00631	0.16122	0.00327	2468	17	2032	19
G2305-1-57	615.53	485.82	669.14	0.7874	5.38031	0.11741	0.24158	0.00527	0.16187	0.00327	2475	17	1882	19
G2305-1-58	142.46	102.87	300.92	0.72464	11.27318	0.26256	0.48442	0.01083	0.16915	0.00371	2549	18	2546	22
G2305-1-59	202.25	154.69	407.64	0.76336	9.46543	0.31987	0.42497	0.01008	0.16154	0.00667	2472	71	2384	31
G2305-1-60	628.17	667.74	675.48	1.06383	5.41816	0.11789	0.24529	0.00534	0.16059	0.00324	2462	17	1888	19
G2305-1-61	362.56	292.42	568.99	0.80645	8.27642	0.17945	0.33708	0.00732	0.17856	0.0036	2640	16	2262	20

(*Continued*)

Table 2. (*Continued*)

spot	[U] ppm	[Th] ppm	[²⁰⁶Pb] ppm	Th/U	²⁰⁷Pb/²³⁵U	± δ%	²⁰⁶Pb/²³⁸U	± δ%	²⁰⁷Pb/²⁰⁶Pb	± δ%	²⁰⁷Pb/²⁰⁶Pb age(Ma)	± δ	²⁰⁶Pb/²³⁸U age(Ma)	± δ
G2305-1-62	89.53	54.05	171.57	0.60241	9.77029	0.30148	0.4019	0.00943	0.17632	0.00683	2619	66	2413	28
G2305-1-63	459.02	314.66	742.58	0.68493	6.46099	0.2258	0.31285	0.00738	0.14978	0.00632	2343	74	2041	31
G2305-1-64	945.79	884.55	668.51	0.93458	4.24663	0.14579	0.16866	0.00405	0.18261	0.00765	2677	71	1683	28
G2305-1-65	317.13	295.42	506.18	0.93458	8.22282	0.29919	0.35325	0.00853	0.16882	0.00737	2546	75	2256	33
G2305-1-66	381.15	292.67	530.59	0.76923	6.82438	0.14734	0.29073	0.00629	0.17081	0.00346	2566	17	2089	19
G2305-1-67	319.46	207.79	472.09	0.64935	6.5096	0.22155	0.3057	0.00716	0.15444	0.00638	2396	72	2047	30
G2305-1-68	346.75	230.01	572.51	0.66225	6.69117	0.21419	0.3172	0.0073	0.15299	0.00603	2380	69	2071	28
G2305-1-69	425.04	283.38	651.8	0.66667	6.97236	0.22982	0.31025	0.00724	0.16299	0.00658	2487	70	2108	29
G2305-1-70	307.18	272.32	308.84	0.88496	5.37103	0.11651	0.23422	0.00506	0.16694	0.00342	2527	17	1880	19
G2305-1-71	612.12	183.39	771.97	0.2994	8.10284	0.17227	0.26831	0.00576	0.21989	0.0044	2980	16	2243	19
G2305-1-72	282.39	127.45	543.91	0.45045	9.26841	0.19813	0.40179	0.00863	0.16797	0.00339	2538	16	2365	20
G2305-1-73	337.07	240.88	654.65	0.71429	8.94349	0.28721	0.39741	0.00919	0.16322	0.00646	2489	68	2332	29
G2305-1-74	157.98	104.61	351.74	0.66225	11.25677	0.24858	0.48413	0.01052	0.16934	0.00356	2551	17	2545	21
G2305-1-75	235.85	184.49	461.94	0.78125	9.89459	0.21119	0.41191	0.00883	0.17497	0.00353	2606	16	2425	20
G2305-1-76	342.16	281.87	419.86	0.82645	6.08611	0.24544	0.27176	0.00665	0.16242	0.00766	2481	82	1988	35
G2305-1-77	427.43	395.73	493.4	0.92593	5.69382	0.2092	0.26383	0.00626	0.15653	0.00685	2418	76	1930	32
G2305-1-78	202.99	128.3	428.05	0.63291	9.73907	0.30934	0.43009	0.00989	0.16423	0.00644	2500	68	2410	29
G2305-1-79	288.21	290.19	418.39	1.0101	6.95787	0.14801	0.31042	0.00663	0.16334	0.00331	2491	16	2106	19
G2305-1-80	231.99	244.45	515.06	1.05263	10.87945	0.23157	0.47761	0.0102	0.16601	0.00337	2518	16	2513	20
G2306-1														
G2306-1-1	208.91	113.11	405.74	0.54054	9.41889	0.20746	0.4083	0.009	0.16795	0.0034	2537	17	2207	41
G2306-1-2	401.09	360.55	437.67	0.9009	4.95385	0.18226	0.21784	0.00533	0.16493	0.00729	2507	76	1270	28
G2306-1-3	499.18	252.69	420.81	0.50505	4.1379	0.13264	0.18392	0.00433	0.16318	0.00649	2489	69	1088	24
G2306-1-4	497.26	164.18	483.09	0.33003	5.08064	0.15321	0.23309	0.0054	0.15809	0.00601	2435	66	1351	28
G2306-1-5	150.47	102.68	281.67	0.68027	11.73235	0.36394	0.45109	0.01075	0.18864	0.00738	2730	66	2400	48
G2306-1-6	137.24	91.48	276.85	0.66667	9.83525	0.22175	0.42843	0.00953	0.16709	0.00349	2529	17	2299	43
G2306-1-7	270.06	202.82	381.21	0.75188	5.87386	0.12905	0.26339	0.0058	0.16232	0.00328	2480	17	1507	30
G2306-1-8	128.08	121.77	274.47	0.95238	10.16784	0.22519	0.44581	0.00985	0.166	0.00339	2518	17	2377	44
G2306-1-9	321.93	273.5	404.69	0.84746	7.18192	0.16276	0.31767	0.00707	0.16454	0.00347	2503	17	1778	35
G2306-1-10	183.67	152.62	377.04	0.83333	10.83022	0.24391	0.47202	0.01049	0.16698	0.00348	2528	17	2492	46

(*Continued*)

Table 2. (*Continued*)

G2306-1-11	177.66	138.43	349.87	0.78125	9.1733	0.20336	0.40358	0.00892	0.16541	0.00338	2512	17	2186	41
G2306-1-12	161.76	99.2	298.71	0.6135	8.69511	0.27024	0.39731	0.00928	0.15873	0.00617	2442	67	2157	43
G2306-1-13	549.22	365.36	532.23	0.66667	4.67355	0.10253	0.2111	0.00465	0.1611	0.00325	2467	17	1235	25
G2306-1-14	219.01	154.09	399.83	0.70423	8.98093	0.19874	0.39116	0.00864	0.16706	0.00341	2528	17	2128	40
G2306-1-15	98.08	67.46	213.71	0.68966	10.79928	0.24214	0.46102	0.01024	0.17044	0.00354	2562	17	2444	45
G2306-1-16	297.08	121.98	306.08	0.40984	4.05346	0.15583	0.21518	0.00517	0.13662	0.00619	2185	81	1256	27
G2306-1-17	182	174.13	355.35	0.95238	9.5923	0.21151	0.41652	0.00919	0.16754	0.0034	2533	17	2245	42
G2306-1-18	470.54	535.83	425.24	1.13636	4.55967	0.10002	0.19379	0.00427	0.17117	0.00346	2569	17	1142	23
G2306-1-19	79.47	15.18	246.42	0.19084	9.26694	0.24755	0.40244	0.00919	0.16701	0.00587	2528	60	2180	42
G2306-1-20	328.99	143.25	521.59	0.43478	8.11783	0.17774	0.34847	0.00767	0.16946	0.00341	2552	17	1927	37
G2306-1-21	815.14	561.03	525.88	0.68966	2.72627	0.12025	0.13029	0.00329	0.15176	0.00771	2366	89	790	19
G2306-1-22	483.51	280.81	1186.15	0.5814	5.70316	0.17043	0.24223	0.00563	0.17076	0.00647	2565	65	1398	29
G2306-1-23	271.4	307.42	407.85	1.13636	7.49986	0.16627	0.32448	0.00718	0.1681	0.00344	2539	17	1812	35
G2306-1-24	161.19	133.81	249.46	0.83333	7.88337	0.17498	0.32872	0.00728	0.17441	0.00358	2600	17	1832	35
G2306-1-25	286.89	198.98	575.34	0.69444	9.65039	0.21086	0.41141	0.00906	0.17058	0.00342	2563	17	2221	41
G2306-1-26	222.29	130.94	456.85	0.58824	9.79803	0.30017	0.43231	0.0101	0.16438	0.00633	2501	66	2316	45
G2306-1-27	570.12	275.74	601.83	0.48309	4.57955	0.1594	0.2179	0.00519	0.15242	0.00643	2373	74	1271	27
G2306-1-28	420.63	310.84	530.13	0.74074	5.85355	0.12922	0.27064	0.00598	0.15726	0.0032	2426	17	1544	30
G2306-1-29	116.41	92.42	258.38	0.79365	10.81992	0.24358	0.47562	0.01058	0.16541	0.00345	2512	17	2508	46
G2306-1-30	181.93	113.12	376.65	0.62112	10.21117	0.22685	0.44317	0.00982	0.16752	0.00344	2533	17	2365	44
G2306-1-31	342.93	107.76	589.99	0.31447	7.94006	0.20537	0.36293	0.00813	0.15867	0.00543	2442	59	1996	38
G2306-1-32	381.9	265.89	620.64	0.69444	7.76519	0.1698	0.34143	0.00752	0.16533	0.00332	2511	17	1894	36
G2306-1-33	118.44	93.94	265.03	0.79365	11.02908	0.24831	0.4803	0.0107	0.16693	0.00348	2527	17	2529	47
G2306-1-34	265.72	17.8	359.97	0.06698	5.93557	0.1386	0.27873	0.0061	0.15445	0.00494	2396	56	1585	31
G2306-1-35	166.16	124.87	382.99	0.75188	10.69635	0.24438	0.47351	0.0106	0.1642	0.00349	2499	17	2499	46
G2306-1-36	320.92	190.2	555.8	0.59172	8.3817	0.25304	0.37065	0.00863	0.16401	0.00625	2497	66	2032	41
G2306-1-37	350.14	259.68	563.12	0.74074	5.43678	0.26302	0.27682	0.00724	0.14245	0.00783	2257	97	1575	37
G2306-1-38	583.71	242.88	689.4	0.41667	4.95063	0.16224	0.22418	0.00529	0.16017	0.00647	2457	70	1304	28
G2306-1-39	262.97	133.17	430.95	0.50761	7.56936	0.17028	0.33352	0.00742	0.16494	0.00344	2507	17	1855	36
G2306-1-40	234.71	255.59	417.14	1.08696	8.10377	0.33914	0.37823	0.00951	0.15539	0.00759	2406	85	2068	45
G2306-1-41	606.62	286.58	655.26	0.4717	4.42355	0.16434	0.21345	0.00515	0.15031	0.00666	2349	78	1247	27
G2306-1-42	532.99	352.8	647.1	0.66225	5.55157	0.17677	0.25792	0.00605	0.15611	0.00617	2414	69	1479	31

(*Continued*)

Table 2. (*Continued*)

spot	[U] ppm	[Th] ppm	[206Pb] ppm	Th/U	207Pb/235U	± δ%	206Pb/238U	± δ%	207Pb/206Pb	± δ%	207Pb/206Pb age(Ma)	± δ	206Pb/238U age(Ma)	± δ
G2306-1-43	272.19	98.5	417.94	0.36232	8.57987	0.2547	0.3844	0.00892	0.16188	0.0061	2475	65	2097	42
G2306-1-44	188.72	143.63	360.33	0.76336	7.98869	0.30992	0.39031	0.00959	0.14845	0.00682	2328	81	2124	44
G2306-1-45	338.76	288.91	567.95	0.8547	8.08781	0.17791	0.35521	0.00785	0.16542	0.00335	2512	17	1959	37
G2306-1-46	180.78	138.66	430.61	0.76923	10.72297	0.24496	0.47413	0.01062	0.1643	0.00349	2500	17	2502	46
G2306-1-47	234.26	163.02	547.1	0.69444	9.07659	0.21074	0.43899	0.00984	0.1502	0.00326	2348	18	2346	44
G2306-1-48	422.76	463.16	669.64	1.0989	7.72654	0.16909	0.34138	0.00753	0.16441	0.00331	2502	17	1893	36
G2306-1-49	293.12	272.64	542.46	0.92593	8.46227	0.18599	0.36762	0.00812	0.1672	0.00338	2530	17	2018	38
G2306-1-50	241.33	347.85	407.32	1.44928	8.36578	0.18626	0.3629	0.00805	0.16744	0.00345	2532	17	1996	38
G2306-1-51	984.07	1100.56	778.34	1.1236	3.265	0.14764	0.16074	0.00409	0.14732	0.00764	2315	91	961	23
G2306-1-52	274.15	318.06	582.33	1.16279	10.46766	0.22918	0.45442	0.01003	0.1673	0.00337	2531	17	2415	44
G2306-1-53	187.21	156.63	366.05	0.83333	9.30901	0.34512	0.42397	0.01037	0.15925	0.00707	2448	77	2278	47
G2306-1-54	426.14	324.38	745.4	0.76336	8.34062	0.18198	0.3722	0.00821	0.16273	0.00326	2484	17	2040	39
G2306-1-55	389.84	393.78	740.93	1.0101	8.78134	0.19151	0.39303	0.00866	0.16225	0.00325	2479	17	2137	40
G2306-1-56	648.77	543.48	864.75	0.84034	6.11415	0.13392	0.27262	0.00602	0.16285	0.00328	2485	17	1554	30
G2306-1-57	492.46	568.22	768.13	1.14943	7.33551	0.16065	0.33109	0.00731	0.16087	0.00324	2465	17	1844	35
G2306-1-58	505.19	294.37	825.09	0.5814	6.99108	0.23241	0.34031	0.00802	0.14899	0.00607	2334	71	1888	39
G2306-1-59	275.65	284.79	586.74	1.03093	10.2626	0.39314	0.44389	0.01102	0.16768	0.00765	2535	78	2368	49
G2306-1-60	295.89	413.31	582.26	1.38889	9.3808	0.2058	0.41208	0.00911	0.16527	0.00334	2510	17	2224	42
G2306-1-61	996.58	1396.81	1049.64	1.40845	5.09006	0.23785	0.22243	0.00584	0.16597	0.00889	2517	92	1295	31
G2306-1-62	229.52	338.31	500.7	1.47059	10.64083	0.23722	0.47218	0.0105	0.16359	0.00337	2493	17	2493	46
G2306-1-63	201.91	134.19	379.56	0.66667	10.3645	0.34182	0.44289	0.01064	0.16973	0.00693	2555	70	2364	48
G2306-1-64	264.96	284.99	637.86	1.07527	11.09625	0.24369	0.48107	0.01064	0.16742	0.00338	2532	17	2532	46
G2306-1-65	345.85	353.71	793.24	1.02041	11.81323	0.25958	0.49448	0.01095	0.1734	0.00351	2591	17	2590	47
G2306-1-66	267.29	358.67	583.33	1.33333	10.53105	0.23477	0.47001	0.01045	0.16261	0.00335	2483	17	2484	46
G2306-1-67	1421.02	2587.73	884.11	1.81818	3.48809	0.07587	0.1446	0.00319	0.17506	0.0035	2607	17	871	18
G2306-1-68	419.49	297.07	1067.34	0.70922	18.0596	0.50916	0.55287	0.01308	0.23691	0.00872	3099	60	2837	54
G2306-1-69	426.95	539.75	718.03	1.26582	8.26478	0.18241	0.3672	0.00813	0.16333	0.00333	2490	17	2016	38
G2306-1-70	740.39	136.83	927.93	0.18484	5.98584	0.15189	0.28769	0.0064	0.1509	0.00509	2356	59	1630	32
G2306-1-71	595.36	885.62	942.56	1.49254	6.49389	0.38524	0.32796	0.00902	0.14361	0.00939	2271	116	1828	44
G2306-1-72	864.65	1217.37	1142.89	1.40845	6.23631	0.136	0.2865	0.00632	0.15794	0.00317	2434	17	1624	32

(*Continued*)

Table 2. (*Continued*)

|														
G2306-1-73	420.31	520.41	730.36	1.23457	10.51459	0.24062	0.46955	0.01054	0.16247	0.00346	2482	18	2482	46
G2306-1-74	977.23	1223.82	1418.93	1.25	6.6115	0.30159	0.31315	0.00803	0.15313	0.00801	2381	91	1756	39
G2306-1-75	1375.04	1341.22	1549.14	0.97087	4.51397	0.20738	0.23372	0.00592	0.14007	0.00735	2228	93	1354	31
G2306-1-76	821.94	666.31	1429.85	0.81301	8.4475	0.18387	0.37788	0.00834	0.16217	0.00324	2478	17	2066	39
G2306-1-77	1186.43	2756.36	1496.18	2.32558	8.28929	0.18432	0.31376	0.00698	0.19165	0.00395	2756	17	1759	34
G2306-1-78	526.62	986.77	1091.63	1.88679	10.85363	0.23758	0.45128	0.00998	0.17446	0.00351	2601	17	2401	44
G2306-1-79	435.27	600.89	780.99	1.38889	7.98323	0.43291	0.4018	0.01078	0.1441	0.00872	2277	107	2177	50
G2306-1-80	1017.27	1999.96	1542.03	1.96078	4.91815	0.45689	0.295	0.00909	0.12092	0.01183	1970	181	1666	45
GCN-1														
GCN-1-1.1	443.06	687.2	189	1.60263	11.98224	1.35288	0.49804	1.29367	0.17449	0.39584	2576	7	2605	34
GCN-1-2.1	544.04	501.45	231	0.95237	11.88828	1.30827	0.49546	1.25657	0.17402	0.36414	2581	6	2594	30
GCN-1-3.1	387.19	421.2	166 .00	1.12401	11.87844	1.3731	0.50066	1.30473	0.17208	0.42787	2560	7	2617	32
GCN-1-4.1	409.86	1155.91	158	2.91403	11.45317	1.3464	0.45669	1.27895	0.18189	0.42081	2543	7	2425	39
GCN-1-5.1	563.65	821.38	207	1.50575	10.06773	1.50417	0.43049	1.45668	0.16962	0.37498	2518	6	2308	34
GCN-1-6.1	438.87	369.54	189	0.87004	11.87616	1.34483	0.50096	1.27396	0.17194	0.4308	2559	7	2618	30
GCN-1-7.1	160.35	79.78	72.4	0.51406	12.10919	2.08966	0.52431	1.96842	0.1675	0.70143	2543	12	2717	46
GCN-1-8.1	647.48	1224.05	151	1.95337	5.80418	1.32022	0.27757	1.24374	0.15166	0.44284	2137	9	1579	23
GCN-1-9.1	289.84	289.38	125	1.03161	12.0925	1.47069	0.50492	1.32017	0.1737	0.64815	2571	11	2635	32
GCN-1-10.1	221.83	216.78	82.8	1.00978	10.29055	1.49342	0.43843	1.36365	0.17023	0.60891	2482	12	2344	30
GCN-1-11.1	30.61	698.47	12.6	23.58102	9.43291	2.96571	0.46414	2.31316	0.1474	1.856	2561	27	2458	110
GCN-1-12.1	744.27	688.72	120	0.95615	3.04558	1.37599	0.18717	1.25278	0.11801	0.5691	1887	13	1106	15
GCN-1-13.1	216.09	427.84	93.7	2.04572	12.16572	1.57305	0.50637	1.44774	0.17425	0.61525	2569	11	2641	41
GCN-1-14.1	463.24	231.38	195	0.5161	11.60832	1.36296	0.48948	1.29035	0.172	0.43893	2577	7	2568	29
GCN-1-15.1	308.61	417.19	130	1.39678	11.75519	1.45593	0.49112	1.34927	0.1736	0.547	2575	9	2576	34
GCN-1-16.1	127.64	95.83	54.9	0.77571	11.89478	1.7833	0.50039	1.5647	0.1724	0.85549	2583	15	2615	37
GCN-1-17.1	294.93	275.08	101	0.96372	9.49608	1.49861	0.40657	1.3651	0.1694	0.61835	2394	14	2199	28
GCN-1-3.2	403.65	483.85	169	1.23857	11.44005	1.43744	0.48719	1.33363	0.1703	0.53634	2546	9	2559	33
GCN-1-1.2	568.73	935.12	228	1.69891	11.25195	1.65005	0.46923	1.56521	0.17392	0.52226	2540	9	2480	40
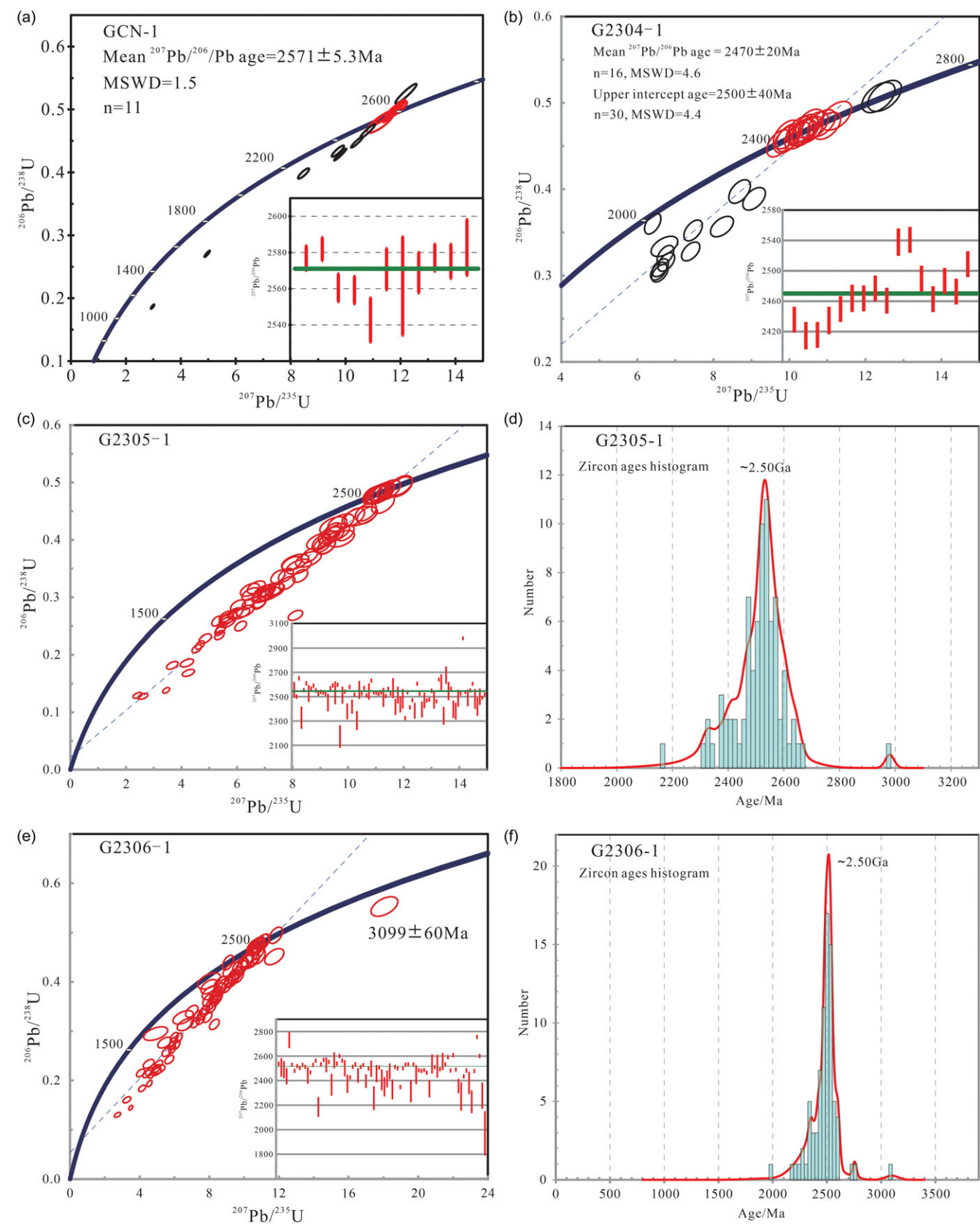
Figure 5. U-Pb concordia diagrams of zircons from supracrustal rocks in the Anshan-Benxi area.
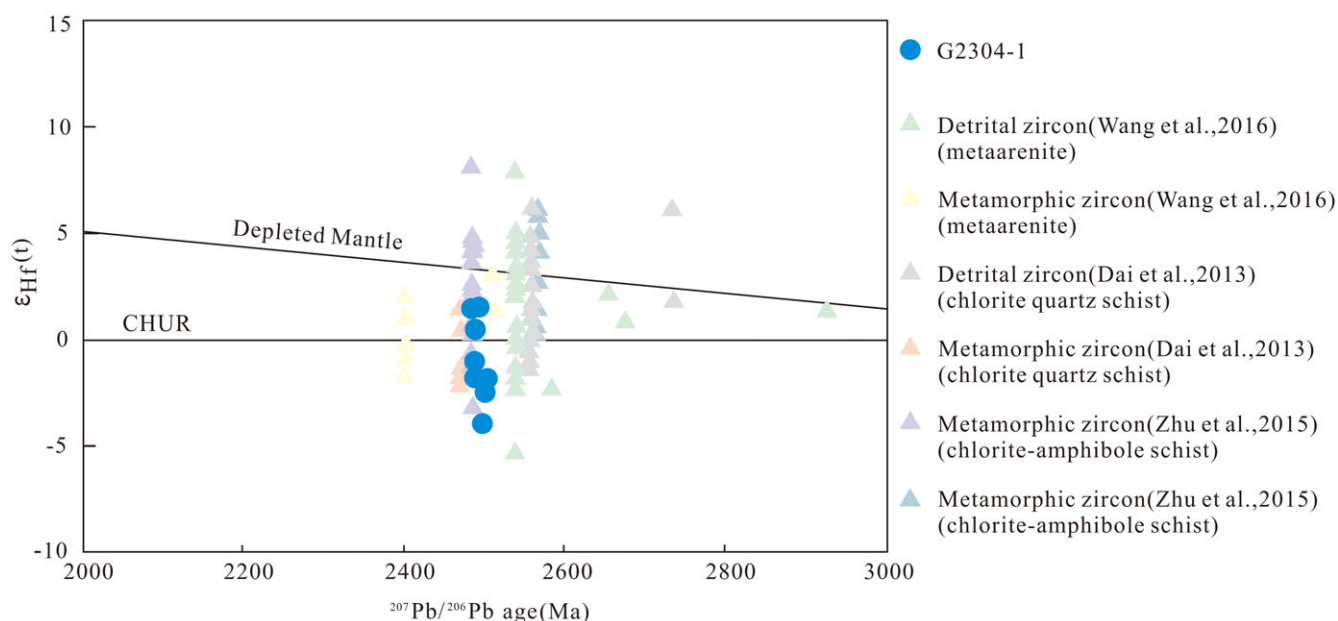
Figure 6. Zircon Age-ε_{Hf}(t) diagram of meta-rhyolite in supracrustal rocks in the Anshan-Benxi area and supracrustal rocks in the Anshan-Benxi area of Zhu *et al.*, 2015, Dai *et al.*, 2013a and Wang *et al.*, 2016.

The rare earth element distribution pattern in sericite quartz schist shows a predominantly right-leaning, with an enrichment of light rare earth elements (Fig. 7c). The total rare earth elements (ΣREE) range from 122.56ppm to 129.16ppm, with $(La/Yb)_N$ values ranging from 9.77 to 9.87, and $(La/Sm)_N$ values ranging from 4.68 to 4.84. The ratio of light to heavy rare earth elements (LREE/HREE) ranges from 9.97 to 10.15, with δEu values ranging from 0.54 to 0.55, indicating a negative anomaly of Eu. Among the trace elements, enrichment is primarily observed in Rb, K, Nd and Th, while Ba, Nb, P and Ti are notably deficient (Fig. 7d).

Meta-rhyolite: SiO_2 contents range from 64.69 to 76.28wt.%, typical of acidic rock. The Al_2O_3 contents range from 14.19 to 17.21wt.%; TiO_2 contents from 0.40 to 0.61wt.%; MgO contents from 0.61 to 3.16wt.%; CaO contents from 0.27 to 1.08wt.%, Fe_2O_{3T} contents from 2.83 to 6.45wt.%, and the total alkali Na_2O+K_2O contents from 5.07 to 6.89 wt.%, with minimal amounts of other oxides. The LOI ranges from 1.96 to 2.81wt.%, $Mg^{\#}$ from 30.03 to 49.98, Rittmann index (σ) from 0.77 to 2.19 (Table 4), indicating that meta-rhyolites are predominantly calc-alkaline rocks, as illustrated in the illustrations (Fig. 8f, h, i). In the TAS (Na_2O+K_2O vs. SiO_2) and SiO_2 vs. Zr/TiO_2 diagrams it falls centrally within the rhyolite region (Fig. 8d, e). Upon comparison of the Al_2O_3, Na_2O+K_2O and Na_2O+K_2O+CaO contents, the rocks are identified as peraluminous, a classification reinforced by their positioning in the ANK-ACNK diagram within the peraluminous region.

The rare earth element partitioning pattern of the meta-rhyolite quarried at Jiajiagoucun shows a predominantly right-leaning, indicating a higher enrichment of light rare earth (Fig. 7c). The ΣREE of the meta-rhyolite ranges from 83.72 ppm to 138.63 ppm, with $(La/Yb)_N$ values ranging from 6.17 to 7.06 and $(La/Sm)_N$ values ranging from 3.65 to 4.20. The LREE/HREE ranges from 7.53 to 9.05, with δEu values ranging from 0.50 to 0.59, signifying a negative anomaly of Eu. Trace elements are primarily enriched in Zr and U and deficient in Ba, Nb, Ti and Sr (Fig. 7d). In the meta-rhyolite extracted from the east of Qianpaifangcun and the south of the Donggou, similar right-leaning patterns of rare earth element partitioning are observed.

The ΣREE values range from 123.77ppm to 165.50ppm, $(La/Yb)_N$ values range from 15.16 to 17.24, with $(La/Sm)_N$ values ranging from 4.61 to 4.87. The LREE/HREE values range from 12.99 to 14.00, and δEu values range from 0.80 to 0.90, showing a weak Eu negative anomaly feature, and the trace elements are mainly enriched in Cs, U, K and Zr, alongside deficiencies in Ba, Nb, Sr and Ti (Fig. 7d).

Meta-sandstone: SiO_2 contents range from 60.85 to 70.92wt.%. The Al_2O_3 contents range from 15.24 to 17.50wt.%; TiO_2 contents from 0.34 to 0.53wt.%; CaO contents from 0.99 to 1.25wt.%, MgO content from 1.31 to 4.37wt.%, Fe_2O_{3T} contents from 3.17 to 7.60wt.%. The total alkali Na_2O+K_2O contents range from 7.29 to 7.83wt.% (Table 4), with relatively low amounts of other oxides present. The LOI ranges from 1.36 to 2.92wt.%, $Mg^{\#}$ varies from 43.21 to 54.88, placing them within the sandstone region in the La/Yb vs.ΣREE diagram (Fig. 8c).

The rare earth element partitioning pattern of meta-sandstones closely resembles that of Post-Archaean Australian average shale (PAAS), the ΣREE range from 142.12 ppm to 146.59 ppm, with $(La/Yb)_N$ ranging from 14.00 to 15.65, $(La/Sm)_N$ ranging from 4.90 to 4.99 (Fig. 7e). The LREE/HREE falls within the range of 11.71 to 12.67, δEu values range from 0.79 to 0.94, indicating a weak negative anomaly of Eu. Furthermore, trace elements in these meta-sandstones are primarily enriched in Ba and Sm while showing deficits in Nb, P, Zr and Tb (Fig. 7f).

Chlorite schist: SiO_2 contents range from 50.21 to 52.99 wt.%, indicating they are of medium basic rock. The Al_2O_3 contents range from 14.30 to 14.64wt.%; TiO_2 contents from 1.21 to 1.32wt.%; CaO contents from 0.16 to 0.19wt.%, MgO contents from 9.94 to 10.29wt.%, Fe_2O_{3T} contents from 21.08 to 23.06 wt.%. The total alkali Na_2O+K_2O contents are very slight at about 0.05wt.%, with low levels of other oxides present. $Mg^{\#}$ ranges from 47.16 to 48.53 (Table 4). In the TAS (Na_2O+K_2O vs. SiO_2) and SiO_2 vs. Zr/TiO_2 diagrams, the chlorite schist falls centrally within the basalt region (Fig. 8d,e). By comparing the magnitude of the Al_2O_3, Na_2O+K_2O and Na_2O+K_2O+CaO contents, the rock is peraluminous, with all of them in the Tholeiitic series (Fig. 8f, h, i).

Table 3. Results of zircon Hf isotope analyses of meta-rhyolite from the Anshan-Benxi area

Sample	age(Ma)	$^{176}Yb/^{177}Hf$	1σ	$^{176}Lu/^{177}Hf$	1σ	$^{176}Hf/^{177}Hf$	1σ	$\varepsilon_{Hf}(t)$	1σ	$t_{DM1}(Ma)$	1σ	$t_{DM2}(Ma)$	1σ	$f_{Lu/Hf}$
G2304-1-01	2464	0.044159	0.000455	0.001471	0.000023	0.281306	0.000023	0.93	0.81	2750.82	31.72	2937.11	52.21	-0.96
G2304-1-02	2464	0.036436	0.000168	0.001176	0.000012	0.281248	0.00002	-0.64	0.7	2808.9	27.33	3037.24	45.32	-0.96
G2304-1-03	2477	0.02924	0.000187	0.000902	0.00001	0.281242	0.000014	-0.11	0.49	2797.05	19	3013.04	31.75	-0.97
G2304-1-04	2552	0.037635	0.001099	0.001292	0.000036	0.281193	0.000002	-0.84	0.7	2892.81	27.37	3117.62	45.33	-0.96
G2304-1-05	2495	0.041667	0.000654	0.001321	0.000022	0.28124	0.000002	-0.48	0.7	2830.58	27.43	3050.93	45.34	-0.96
G2304-1-06	2538	0.035895	0.000263	0.001182	0.000013	0.281211	0.000026	-0.32	0.91	2859.91	35.5	3073.74	58.95	-0.96
G2304-1-07	2541	0.028197	0.000678	0.000985	0.000033	0.281175	0.000002	-1.19	0.7	2894.14	27.15	3131.74	45.31	-0.97
G2304-1-08	2490	0.035926	0.000332	0.00115	0.000018	0.28129	0.000019	1.47	0.67	2749.59	25.98	2922.18	43.17	-0.97
G2304-1-09	2487	0.020187	0.000235	0.000723	0.000012	0.281202	0.000017	-1	0.6	2838.12	22.94	3077.86	38.51	-0.98
G2304-1-10	2509	0.025521	0.000459	0.000852	0.000014	0.281225	0.000032	0.09	1.12	2816.46	43.34	3024.98	72.57	-0.97

The rare earth element partitioning pattern of the chlorite schist is mainly flat, with insignificant enrichment of light rare earth (Fig. 7a). The ΣREE ranges from 86.29ppm to 90.58ppm, with $(La/Yb)_N$ values ranging from 1.97 to 2.34 and $(La/Sm)_N$ values ranging from 1.35 to 1.50. The LREE/HREE ranges from 2.34 to 2.65, and δEu values range from 0.77 to 0.79, indicating a weak negative Eu anomaly. Furthermore, trace elements in these chlorite schist samples are mainly enriched in Rb, U, La, Nd, Sm and Dy, while showing deficits in Ba, K, Sr, Zr and Ti (Fig. 7b).

Actinolite schist: SiO_2 contents range from 40.38 to 49.92 wt.%, indicating they are within the range of basic-ultrabasic rocks. The Al_2O_3 contents range from 11.09 to 15.72 wt.%; CaO contents from 0.07 to 0.17wt.%, Fe_2O_{3T} contents from 27.90 to 29.13wt.%, total alkali Na_2O+K_2O contents from 0.05 to 0.30wt.%, TiO_2 contents from 0.55 to 1.03 wt.%; MgO contents from 9.60 to 13.65wt.%, with other oxides contents are minimal. $Mg^{\#}$ ranges from 47.16 to 48.53 (Table 4). In the TAS (Na_2O+K_2O-SiO_2) and SiO_2 vs. Zr/TiO_2 diagrams, the actinolite schist falls centrally within the tholeiitic region (Fig. 8d,e). All of them show a series of tholeiitic (Fig. 8f, h, i), which are determined to be peraluminous through a comparison of the magnitude of Al_2O_3, Na_2O+K_2O and Na_2O+K_2O+CaO contents.

The rare earth element partitioning pattern of actinolite schist is mainly flat, with insignificant enrichment of light rare earth (Fig. 7a). The samples exhibit obvious U-positive anomalies, Rb-positive anomalies, Sr-negative anomalies and Ti-negative anomalies (Fig. 7b). The ΣREE ranges from 23.16ppm to 41.55ppm, with $(La/Yb)_N$ values ranging from 0.59 to 1.21 and $(La/Sm)_N$ values ranging from 0.73 to 1.13. The LREE/HREE ranges from 1.45 to 1.98.

Amphibolite: SiO_2 contents range from 40.82 to 53.61wt.%, which places them in the category of basic rocks. The Al_2O_3 contents range from 9.6 to 15.25wt.%; TiO_2 contents from 0.39 to 0.52wt.%; CaO contents from 0.23 to 8.22wt.%, MgO contents from 5.68 to 10.89wt.%, Fe_2O_{3T} contents from 13.29 to 34.19wt.%, total alkali Na_2O+K_2O contents from 0.3 to 4.59wt.%, while other oxide contents are low. $Mg^{\#}$ contents range from 38.91 to 58.09 (Table 4). The samples fall into the region of amphibolite in the La/Yb-ΣREE diagram (Fig. 8c). The rock is identified as peraluminous, in addition, tholeiitic basalt series by comparing the magnitude of Al_2O_3, Na_2O+K_2O and Na_2O+K_2O+CaO contents (Fig. 8f, h, i). In the MgO-CaO-FeO_T diagram, amphibolite falls into ortho-amphibolite, indicating that the protolith of amphibolite is igneous rock, which is further supported in the TiO_2 vs. SiO_2 diagram (Fig .8b, g).

The rare earth element partitioning pattern of amphibolite is mainly flat, with insignificant enrichment of light rare earth elements (Fig. 7a). The ΣREE ranges from 25.44ppm to 56.23ppm, with $(La/Yb)_N$ values ranging from 0.72 to 3.05, $(La/Sm)_N$ values ranging from 0.86 to 2.42. The LREE/HREE ranges from 1.16 to 3.44, and δEu values range from 0.61 to 1.12, indicating a weak negative Eu anomaly. The trace elements are primarily enriched in Rb and K, while deficient in Ba, Sr and Ti (Fig. 7b).

6. Discussion

6.a. Distribution and formation age of supracrustal rocks

Archaean supracrustal rocks are extensively exposed in the NCC. Towards the end of the Neoarchaean period, the magmatic activity in the NCC intensified, accompanied by metamorphism. In the Jidong area, Xiang *et al.* (2012) conducted zircon U-Pb dating on amphibolite, the surrounding rock of the Zhoutaizi iron ore mine
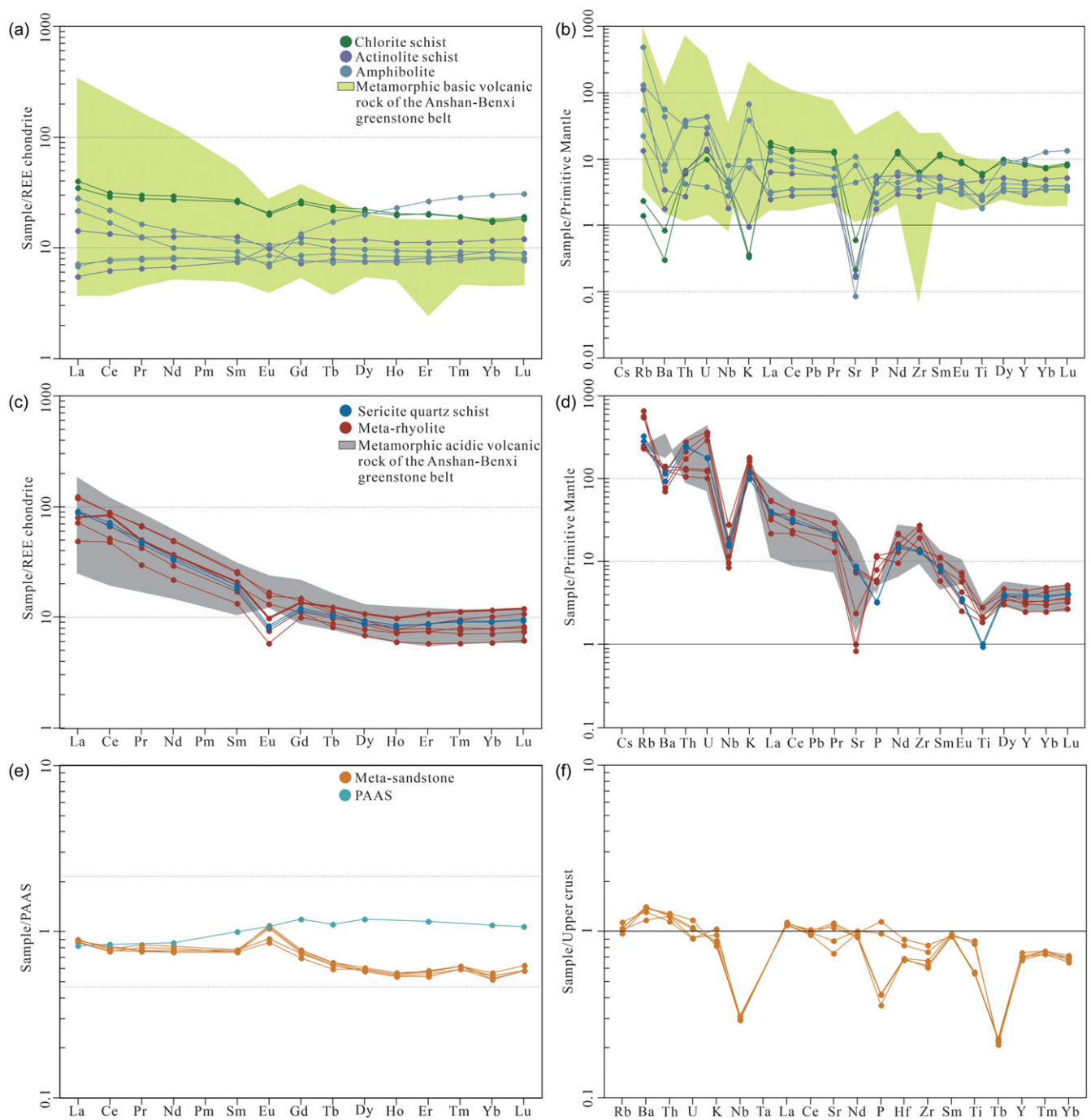
Figure 7. Chondrite normalized REE (a,c: normalized values after Boynton 1984), and primitive mantle normalized spider diagrams (b,d: normalized values after Sun and McDonough 1989) of sericite quartz schist, meta-rhyolite, chlorite schist, actinolite schist and amphibolite in the Anshan-Benxi area; PAAS-normalized REE patterns (e: normalized value after McLennan, 1989) and upper crust-normalized trace element spider diagram (f: normalized value after Taylor and McLennan, 1985) of meta-sandstones in the Anshan-Benxi area. (a,b) Metamorphic basic volcanic rock; (c,d) Metamorphic acidic volcanic rock; (e,f) Meta-sandstone.

in Luanping County. The results revealed that the upper intercept age of magmatic zircon was 2512 ± 21 Ma, representing the volcanic eruption and precipitation of the BIF in the Zhoutaizi iron ore deposit. Additionally, the weighted average age of metamorphic zircon was determined to be 2394 ± 21 Ma, suggesting the timing of metamorphic event in the Zhoutaizi iron ore deposit, which led to the alteration of the protoliths and ores. Additionally, $\varepsilon_{Hf}(t)$ values and two- stage depleted mantle model age indicated that the magma source region was subjected to mingling by ancient

crustal materials; Zhang *et al.* (2011) carried out zircon U-Pb dating on amphibolite gneisses intercalated with the Shuichang iron ore deposit. The findings revealed volcanic activity at 2547 ± 7 Ma and metamorphism at 2513 ± 4 Ma in the area. Based on the geochemical characteristics of the surrounding rocks, it was inferred that it formed a back-arc basin associated with subduction.

In the Fushun and Qingyuan regions of Liaoning, SHRIMP zircon U-Pb age determinations conducted by Wan *et al.* (2005) of the Archaean amphibolite yielded a magmatic zircon weighted
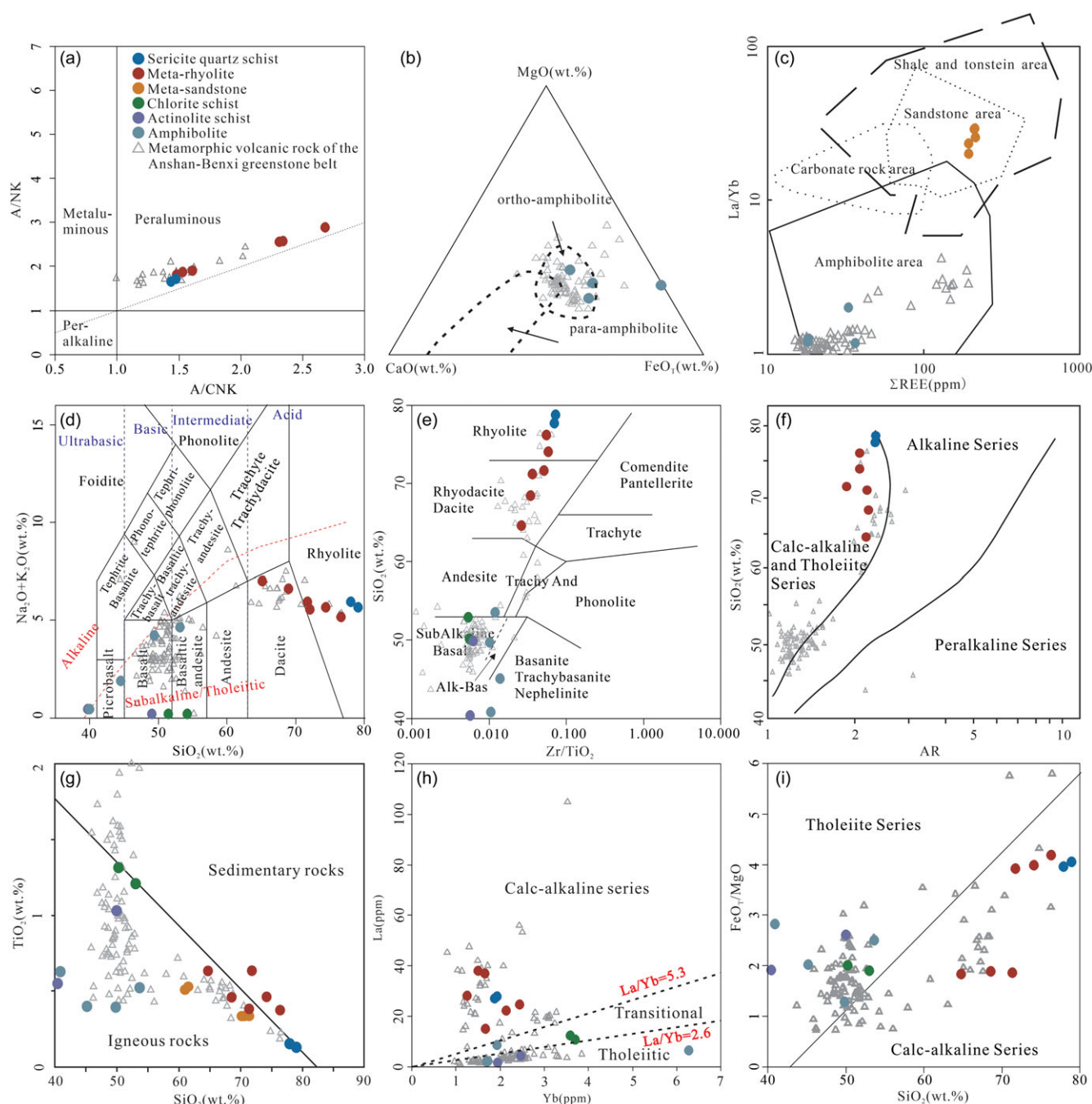
Figure 8. (a) A/CNK-A/NK diagram (Shand, 1943); (b) MgO-CaO-FeO$_T$ diagram (Walker *et al.*, 1959); (c) La/Yb-ΣREE diagram (Gromet *et al.*, 1984); (d)TAS diagram (Bas *et al.*, 1986); (e) SiO$_2$ vs. Zr/TiO$_2$ diagram (Winchester and Floyd, 1977); (f) SiO$_2$ vs. AR diagram (Wright, 1969); (g) TiO$_2$ vs. SiO$_2$ diagram (Tarney, J., 1976); (h) La vs. Yb diagram (Ross and Bédard, 2009); (i) FeO$_T$/MgO vs. SiO$_2$ diagram (Miyashiro, 1974) of supracrustal rocks in the Anshan-Benxi area.

average age of 2515 ± 6 Ma for the hornblende metamorphic granulites of the Xiaolaihe Iron Ore Mine Area, 2510 ± 7 Ma for the hornblende metamorphic granulites of the Fushun Tangtu and 2479 ± 5 Ma for the hornblende metamorphic granulite metasedimentary zircon age of the Qingyuan Group in the northern part of Qingyuan. These results suggest a significant tectonic-thermal event during the Late Palaeozoic, likely occurring in an island arc setting. Further LA-ICP-MS zircon U-Pb isotope analyses of amphibolite in the eastern Tangtu area by Bai *et al.* (2014) revealed a minimum age of magma crystallization of 2530 ± 5 Ma (Bai *et al.*, 2014). In the Banshigou area of Baishan, Li *et al.*

(2016) conducted zircon U-Pb dating on amphibolite and hornblende schist in the Banshigou crustal rocks. The results showed that amphibolite magmatic zircons were formed at 2548 ± 11 Ma, while epidote hornblende schistic magmatic zircons were formed at 2548 ± 23 Ma, indicating the age of crustal rock formation in an island arc environment. In the Guyang area, Liu *et al.* (2012) carried out SIMS U-Pb dating on amphibolite in the surrounding rock of the Sanheming iron deposit, revealing an upper intersection age of the zircon core is 2562 ± 14 Ma, suggesting formation in a back-arc basin with a tectonic environment of mantle plume superposition.

Based on the information provided, it can be inferred that most of the supracrustal rocks in the NCC were formed around 2500 Ma, underwent late-stage metamorphism and originated in island arc environments. The age determinations indicate that amphibolite (GCN-1) of this study was dated at the age of 2571 ± 18 Ma, meta-rhyolite (G2304-1) at the age of 2470 ± 20 Ma, additionally, two meta-sandstone samples (G2305-1, G2306-1) display a prominent peak at 2500 Ma, indicating that the supracrustal rocks in the Anshan-Benxi area were formed during the Late Neoarchaean. Furthermore, an early detrital zircon with an age of 3099 ± 60 Ma was found in the meta-sandstone (G2306-1), indicating the presence of older rocks in the source region. The contemporaneous formation of supracrustal rocks in the Anshan-Benxi area as well as in Jidong, Fushun, Liaoning, Qingyuan, Baishan Banshigou and Guyang, implies a significant magmatic event during the Late Neoarchaean in the NCC (2550 Ma~2500 Ma).

6.b. Assessments of element mobility

The volcanic rocks in the Anshan-Benxi area have experienced multiple stages of deformation until greenschist metamorphism. This process can alter the activity of certain elements, rendering them unreliable as diagenetic indicators of the protoliths. Therefore, it is crucial to assess the element activity of these metavolcanic rocks to comprehend their petrogenesis and the tectonic context of the Anshan-Benxi area. Polat and Hofmann (2003) discussed the element activity of rocks that have experienced intermediate and high-level metamorphism, in case where the LOI of the sample exceeds 6% and Ce exhibits significant anomalies (Ce*>1.1 or &<0.9), which indicates considerable impact from later alteration or other thermal events. Additionally, when the correlation coefficient (R) with immobile components Al_2O_3/TiO_2 and Zr is above 0.75, the element is considered relatively stable and unaffected by subsequent thermal events.

The LOI of metamorphic acidic rocks ranges from 1.24 to 2.81, all less than 6%, with Ce* values ranging from 0.91 to 1.03 (except for G2303-2-1 and G2303-2-2, whose Ce* are 1.29 and 1.22 respectively). The chondrite normalized REE spider diagrams of chondrites show no discernible Ce anomalies, suggesting that the original chemical composition of metamorphic acidic rocks has not been significantly modified by later events (Polat and Hofmann, 2003). Element covariation diagrams with immobile components Al_2O_3/TiO_2 and Zr demonstrate a strong linear trend for SiO_2, TiO_2, Al_2O_3, CaO, Na_2O, K_2O, as well as Rb, Nb, Yb, Hf and Sr in metamorphic acidic rocks (Fig. 9), with correlation coefficients close to 1, indicating that these elements are relatively immobile during post-magmatic alteration. These elements, along with REEs and HFSE, are chosen to represent the original magma components for analysing the origin of metamorphic acidic rocks and the geodynamic process.

The LOI of metamorphic basic rocks is relatively high, ranging from 1.94 to 7.33, with most exceeding 6%. Covariation diagrams of elements with immobile components Al_2O_3/TiO_2 and Zr reveal a strong linear trend for TiO2, K2O and Hf in metamorphic basic rocks (Fig. 9), with a correlation coefficient close to 1. Due to the protoliths above formed by the metamorphism of basic rocks, unstable elements (such as K, Na, Rb, Sr, etc.) are prone to migrate during alteration and metamorphism, while high-field-strength elements (such as Zr, Hf, Nb, Ta, Ti, Y, etc.) and rare earth elements can remain stable during alteration and metamorphism. This study therefore focuses on elements with high stability to discuss the geological background and origin of the rocks.

6.c. Tectonic environment and petrogenesis of supracrustal rocks in the Anshan-Benxi area

6.c.1. Metamorphic acidic rocks

The metamorphic rhyolite and sericite quartz schist found in the Anshan-Benxi area exhibit relatively high SiO_2 (64.69~78.89wt.%) and Al_2O_3 (12.38~17.21wt.%) and lower MgO (0.4~3.16wt.%) and Mg# (30.03~49.48). Its protolith is equivalent to calc-alkaline rhyolite (Fig. 8d, e). This group of samples has a high $(La/Yb)_N$ ratio (6.17~17.24), and the normalized rare earth element distribution pattern of chondrites is right-leaning. The total amount of rare earth elements is high (122.56 ppm~165.50 ppm), enriched in light rare earth elements, developing obvious negative anomalies of Nb and Ti. These characteristics align closely with typical island arc volcanic rocks, indicating a probable origin associated with an island arc magma environment.

To further corroborate this interpretation, tectonic setting discrimination diagrams were employed. In the Rb/30-Hf-3Ta, R1-R2, Rb-Y+Nb, Nb-Y, Rb-Ta+Yb, Ta-Yb tectonic setting discrimination diagrams (Fig. 10), a significant portion of metamorphic acidic rocks were classified within the categories of volcanic arc granite and syn-collision granite. It was judged that the protolith of this type of rock likely formed within an island arc environment linked to subduction processes.

Zircon Lu-Hf isotopes serve as a relatively valuable tool for tracing magma sources. The Hf isotope test results of metamorphic rhyolite (G2304-1) reveal that εHf(t) ranges from -1.19 to 1.47, intersecting the CHUR evolution line and extending to the DM line on the age-εHf(t) diagram. The two- stage depleted mantle model age, t_{DM2}(Ma), falls within the range of 2922 to 3132Ma, surpassing the zircon formation age of 2500 Ma. The Na/Yb value of metamorphic acidic rocks ranges from 9.92 to 15.22 (with an average of 13.30), which closely aligns with the typical Earth's crust (11~12, Green, 1994); the Zr/Hf ratio ranges from 32.29 to 40.56, with an average value of is 37.31, indicating values higher than the average Zr/Hf value of crust-derived magma (33, R. G, 1985; Zhang et al., 2021), but lower than that of mantle-source magma (39, Zhang et al., 2020). These findings suggest that the metamorphic acidic protolith magma in the study area likely originated from the partial melting of the 3.0 Ga basaltic crust. The observation of high Mg# in metamorphic acidic rocks implies that the addition of mantle components to the protolith during its diagenesis, corroborated by its extension towards the mantle end-member on the age-εHf(t) diagram. In conclusion, it is speculated that the metamorphic acidic rocks in the Anshan-Benxi area may have originated from the partial melting of 3.0Ga basaltic crust, supplemented with lithospheric mantle contributions.

6.c.2. Metamorphic basic rocks

The chondrite normalized rare earth element distribution pattern of the chlorite schist, actinolite schist and amphibolite in the Anshan-Benxi area of metamorphic basic rocks exhibits flat, lacking significant enrichment in light rare earth elements but showing enrichment in Cs and depletion in Sr, Ti and K. Utilizing tectonic setting discrimination diagrams to identify them, they fall into the island arc basalt and mid-ocean ridge tholeiitic basalt in Fig. 11. In the tectonic setting discrimination diagrams of Hf/3-Th-Nb/16, Zr-Ti, 10MnO-TiO₂-10P₂O₅ and Zr/4-2Nb-Y, metamorphic basic rocks fall into island arc tholeiitic basalt, island arc calc-alkaline basalt, depleted mid-ocean ridge tholeiitic basalt and the transitional zone between depleted mid-ocean ridge basalt and island arc basalt (Fig .12). Further geochemical analysis reveals that
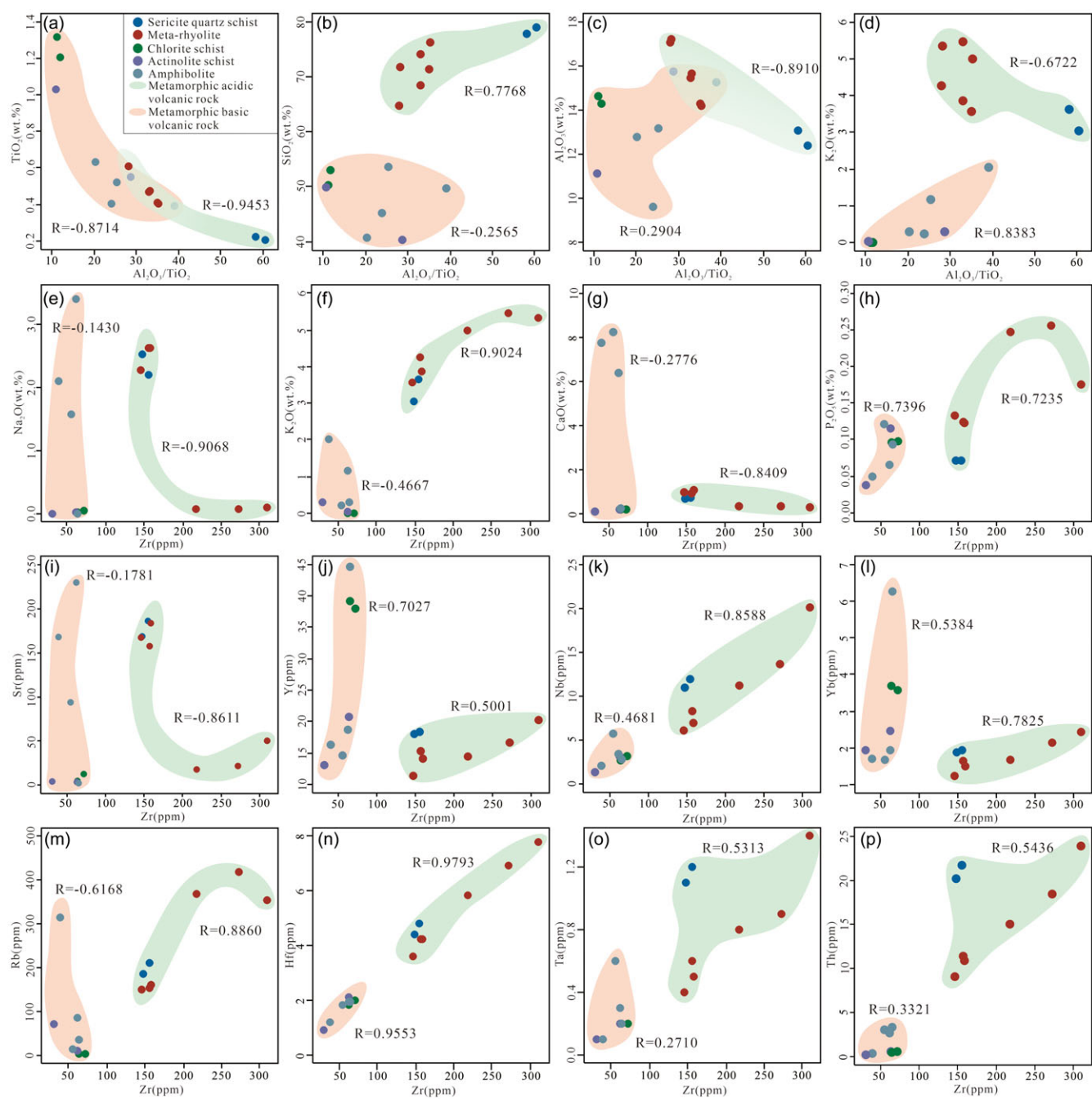
**Figure 9.** Al_2O_3/TiO_2 and Zr vs. selected elements variation diagrams for supracrustal rocks in the Anshan-Benxi area.

the Th (0.51~3.32) of metamorphic basic rocks surpass Ta (0.1~0.6), while the TiO_2 content remains relatively low (0.39~1.32%), which is consistent with the characteristics of island arc basalt (Yang *et al.*, 2016).

The geochemical characteristics of metamorphic basic rocks in the Anshan-Benxi area exhibit elevated Mg# values ranging from 40.77 to 58.09, closely resembling the Mg# value of mid-ocean ridge tholeiitic basalt (60±, BEARD and LOFGREN, 1991). Additionally, the average Nb/Ta radio is 14.17, and the average Zr/Hf radio is 33.24, comparable to the primitive mantle values (Nb/Ta = 17.5, Zr/Hf = 36.27) and higher than the average continental crust values (Nb/Ta = 11, Zr/Hf = 33) (Stolz *et al.*, 1996; Taylor and McLennan, 1985). The average Th/La ratio

stands at 0.19, significantly lower than the average continental crust ratio of 0.28 but marginally higher than the Th/La ratio of the lower crust (0.15), indicating that the basic rock magma was less heavily contaminated by the crust during its ascending emplacement process. Therefore, it can be judged that the protolith of metamorphic basic rock in the Anshan-Benxi area is basaltic volcanic rock, primarily derived from the mantle with limited crustal contamination.

6.c.3. Metamorphic sandstone
The geochemical composition of meta-sandstone plays a crucial role in deciphering the tectonic setting of its formation. By scrutinizing certain trace element contents and ratios,
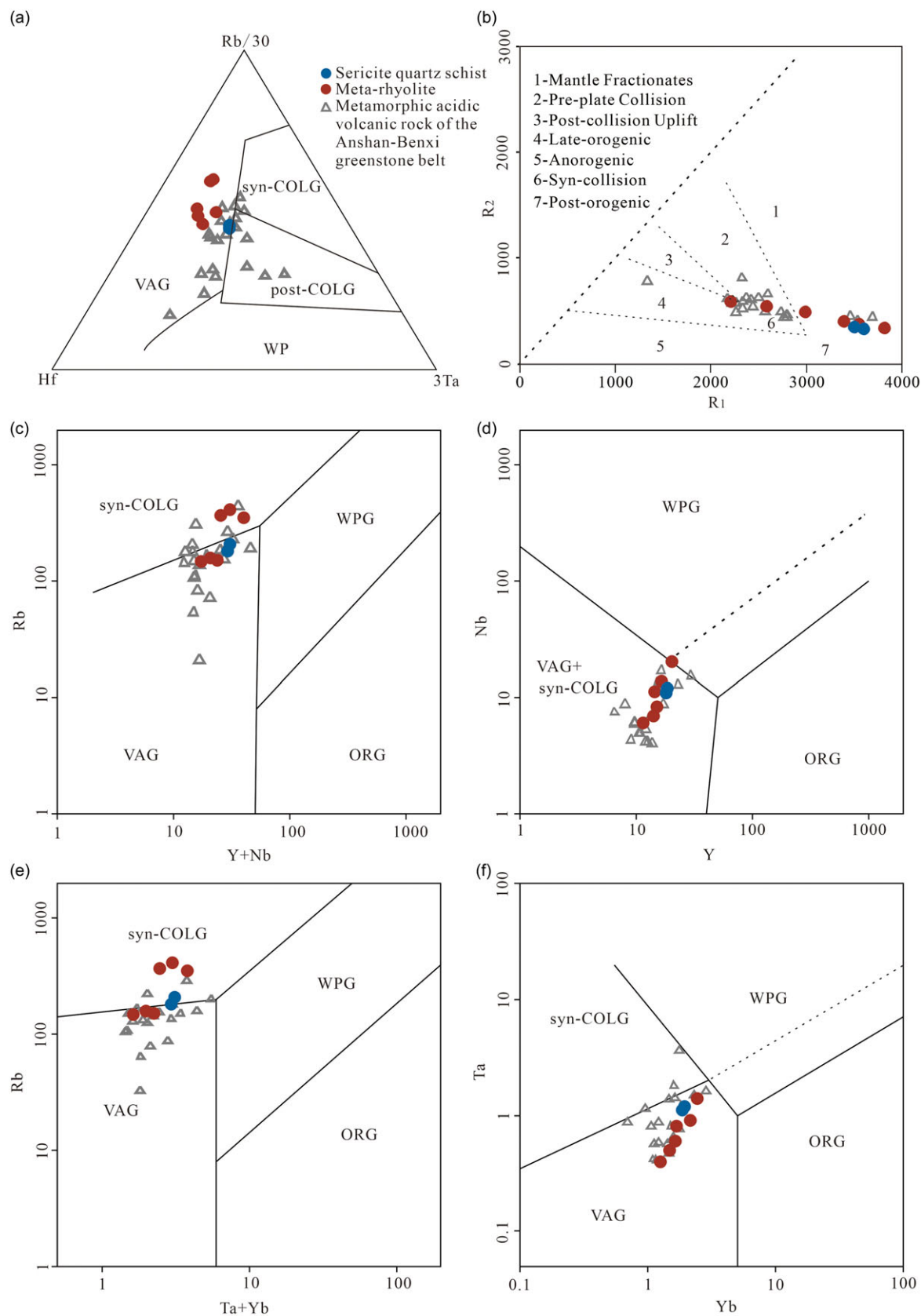
Figure 10. Tectonic setting discrimination diagrams of metamorphic acidic volcanic rocks in the Anshan-Benxi area. (a) Rb/30-Hf-3Ta, after Harris *et al.*, 1986; (b) R_1-R_2, $R_1 = 4Si-11(Na+K)-2(Fe+Ti)$, $R_2 = 6Ca+2Mg+Al$, after Batchelor + Bowden, 1985; (c) Rb-Y+Nb; (d)Nb-Y; (e) Rb-Ta+Yb; (f) Ta-Yb, after Pearce *et al.*, 1984.
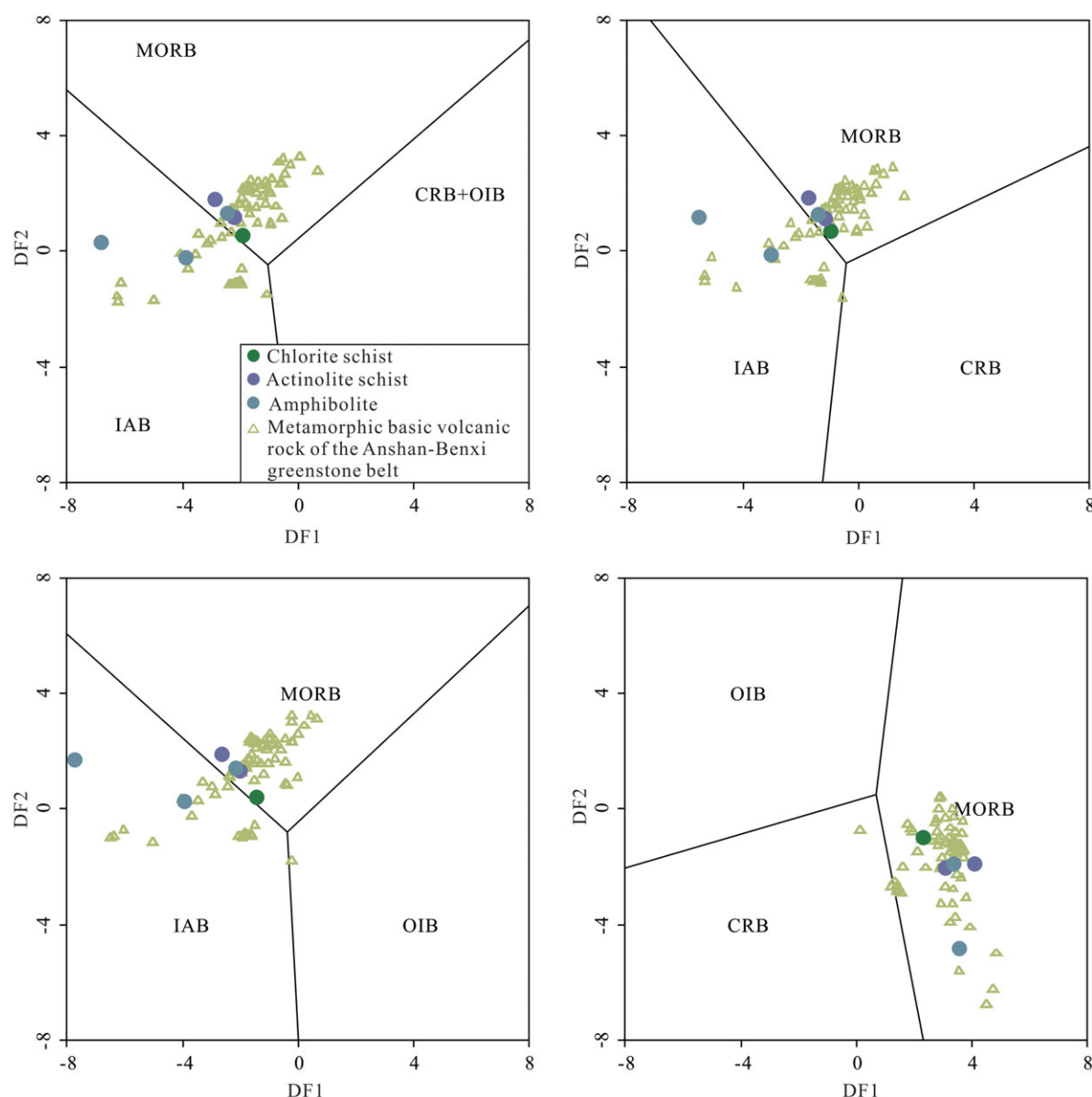
Figure 11. Tectonic setting discrimination diagrams of metamorphic basic volcanic rocks in the Anshan-Benxi area (Agrawal *et al.*, 2008).

researchers can deduce the tectonic setting of the original sedimentary rock formation. Bhatia (1983), Bhatia and Crook (1986) and McLennan and Taylor (1991) utilized this information to categorize the geotectonic environment into four distinct tectonic settings: oceanic island arcs, continental island arcs, active continental margins and passive continental margins. Through a comparative analysis of meta-sandstones from the Anshan Group with those from diverse tectonic environments using the aforementioned theory, it becomes apparent that the La, Ce and ΣREE contents in the meta-sandstones of the Anshan Group closely resemble those found in the continental island arc. Additionally, the trace elements and ratios exhibit a remarked similarity or consistency with those characteristic of the continental island arc (Table 5). The key distinguishing parameters in the meta-sandstones of the Anshan Group overwhelmingly resemble the distinctive characteristic parameters of the

continental island arc, as evidenced by the Zr-Th and La-Th tectonic diagrams (Fig. 13) Therefore, it can be inferred that the protolith of the meta-sandstones in the Anshan Group were deposited by an island arc.

In recent years, the existence of plate movement in the Archaean has become a pivotal scientific inquiry and a subject of considerable debate within Precambrian research. Some scholars posited that plate movement commenced in the Neoarchaean, with the magmatic activity towards the end of the Neoarchaean originating from the base intrusion of the mantle column. Conversely, recent studies offer a contrasting viewpoint. They propose that plate tectonics were already in operation at the end of the Archaean, and the magmatic occurrences at the end of the Neoarchaean magmatic period were the result of arc-continent and continent-continent collisions. Drawing from previous opinions and the findings of this study, it is postulated that the metamorphic
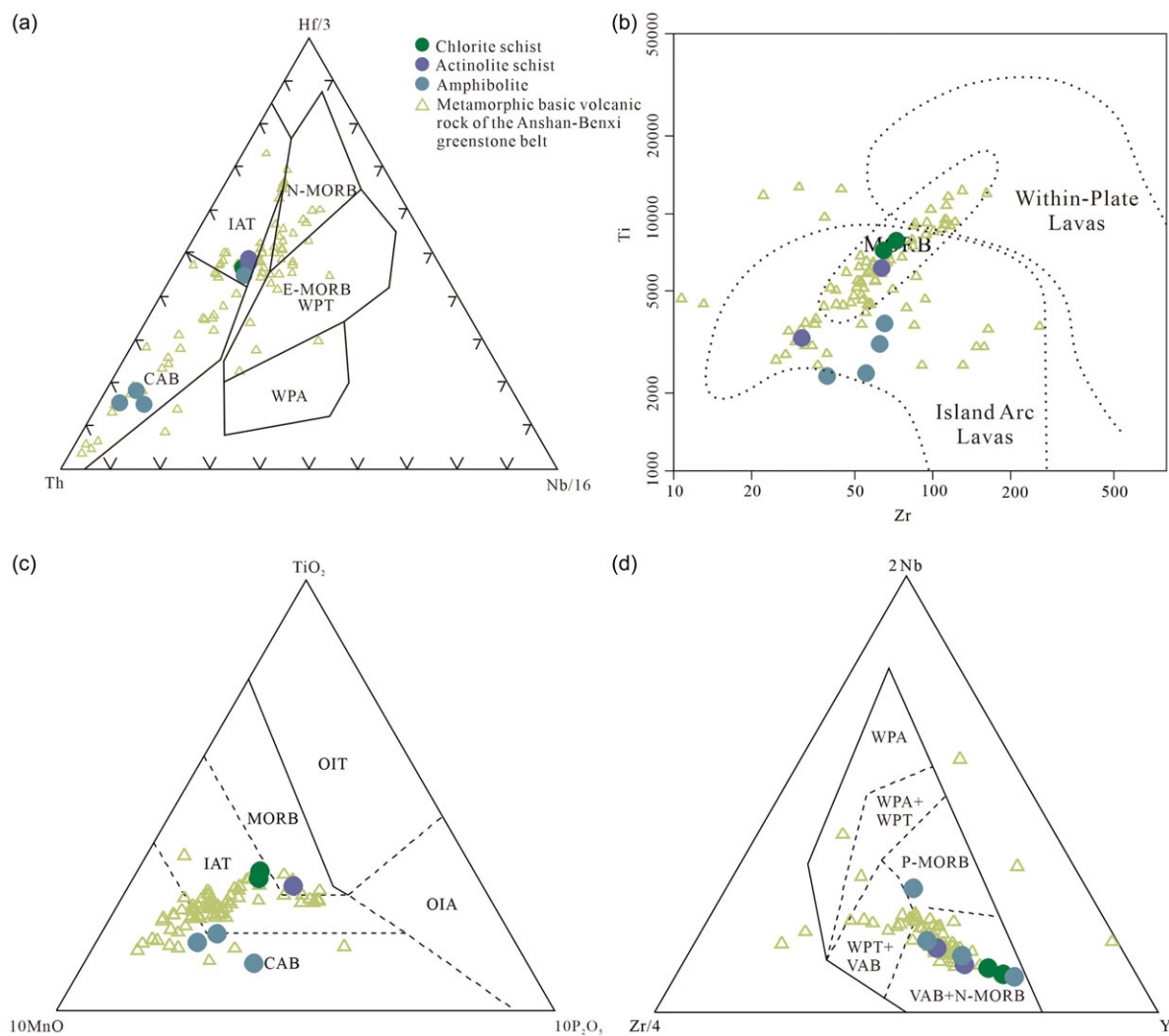
Figure 12. Tectonic setting discrimination diagrams of metamorphic basic volcanic rocks in the Anshan-Benxi area. (a) Hf/3-Th-Nb/16, after Wood, 1980; (b) Zr-Ti, after Pearce, 1982; (c) 10MnO-TiO$_2$-10P$_2$O$_5$, after Mullen, 1983; (d) Zr/4-2Nb-Y, after Meschede, 1986.

acidic rocks in the Anshan-Benxi area may have originated from the partial melting of 3.0Ga basaltic crust, possibly contaminated with lithospheric mantle materials. The protoliths of the metamorphic basic rocks are believed to be basaltic volcanic rocks, deriving from the mantle, without obvious crustal contamination. Tectonic setting discrimination diagrams indicate that the supracrustal rocks in the Anshan-Benxi area originated in island arc and mid-ocean ridge environments, comprising a blend of structural melange through plate subduction, thus bolstering the argument for plate tectonics during the Late Neoarchaean period. In conclusion, the Late Neoarchaean magmatism events in the Anshan-Benxi area of the northeastern NCC formed in an arc tectonic setting associated with plate subduction.

7. Conclusions

Based on zircon U-Pb geochronology, geochemistry and Hf isotope analysis of the supracrustal rocks in the Anshan-Benxi area of northeastern NCC, the following conclusions can be drawn:

(1) Magmatic zircons in the amphibolite of the Anshan Group in the Anshan-Benxi area formed at 2571 ± 18 Ma and the meta-rhyolite magmatic zircons formed at 2470 ± 20 Ma. Additionally, the two meta-sandstone samples show a peak at 2500 Ma, respectively, indicating that the supracrustal rocks in the Anshan-Benxi area were formed in the Late Neoarchaean.

(2) The protolith compositions of sericite quartz schist and metamorphic rhyolite are acidic rhyolite volcanic rock, with magma originating from the partial melting of 3.0Ga basaltic crust. In contrast, the protoliths of actinolite schist, chlorite schist and amphibolite are basaltic volcanic rocks, primarily deriving from mantle sources.

(3) Supracrustal rocks in the Anshan-Benxi area were formed within an island arc and mid-ocean ridge environment, representing a structural melange formed by plate subduction. The Late Neoarchaean magmatism observed in the Anshan-Benxi area in the northeastern part of the NCC occurred within an arc tectonic environment associated with plate subduction.

Table 4. Analysis results of major and trace elements

Sample	G2302-1-1	G2302-1-2	G2303-1-1	G2303-1-2	G2303-1-3	G2304-1-1	G2304-1-2	G2304-1-3	G2305-1-1	G2305-1-2	G2305-1-3	G2306-1-1	G2306-1-2	G2307-1-1	G2307-1-2	P17b6-1	ZC-8	P18b1-2	P18b1-1	GCN-1	HM-7
Intrusion	Jiajiagou		Jiajiagou			East of Qianpaifangcun, the south of Donggou			South of Qianpaifangcun			Donggou		Hujiamiaozi		Gongchangling		Gongchangling			Hujiamiaozi
Petrology	Sericite quartz schist		Meta-rhyolite						Meta-sandstone					Chlorite schist		Actinolite schist		Amphibolite			
SiO_2	77.82	78.89	71.72	76.28	74.09	64.69	68.49	71.29	70.92	70.05	70.46	61.22	60.85	50.21	52.99	49.92	40.38	45.13	53.61	49.77	40.82
TiO_2	0.22	0.2	0.61	0.4	0.47	0.61	0.47	0.41	0.34	0.34	0.34	0.51	0.53	1.32	1.21	1.03	0.55	0.4	0.52	0.39	0.63
Al_2O_3	13.04	12.38	17.21	14.19	15.63	17.07	15.46	14.3	15.24	16.05	15.78	17.5	17.48	14.64	14.3	11.09	15.72	9.6	13.17	15.25	12.76
FeO	0	0	0	0	0	0	0	0	0	0	0	0	0	0	0	11.81	13.13	10.72	6.9	5.5	13.94
Fe_2O_3																17.87	17.79	14.68	9.93	8.66	22.5
Fe_2O_{3T}	1.84	1.8	3.7	2.83	2.96	6.45	5.3	4.73	3.51	3.17	3.22	7.18	7.6	23.06	21.08	27.9	29.13	23.93	15.83	13.29	34.19
MnO	0.03	0.03	0.03	0.02	0.02	0.08	0.06	0.06	0.04	0.03	0.04	0.08	0.08	0.17	0.17	0.13	0.15	0.2	0.17	0.16	0.09
MgO	0.42	0.4	0.85	0.61	0.67	3.16	2.52	2.27	1.33	1.32	1.31	4.37	4.57	10.29	9.94	9.6	13.65	10.58	5.68	9.21	10.89
CaO	0.71	0.66	0.27	0.35	0.35	0.93	1.08	0.97	1.25	1.14	1.06	1.18	0.99	0.16	0.19	0.17	0.07	8.22	6.37	7.73	0.23
Na_2O	2.21	2.53	0.09	0.06	0.08	2.62	2.62	2.27	4.61	4.94	4.92	4.38	4.53	0.04	0.03	0.02	0.01	1.59	3.42	2.1	0.01
K_2O	3.64	3.03	5.35	5.01	5.46	4.27	3.87	3.57	2.69	2.9	2.8	3.42	3.16	0.01	0.01	0.03	0.29	0.22	1.17	2.03	0.29
P_2O_5	0.07	0.07	0.18	0.25	0.26	0.12	0.12	0.13	0.07	0.07	0.06	0.17	0.2	0.1	0.1	0.12	0.04	0.12	0.07	0.05	0.09
CO_2																0.2	0.2	0.3	0.2	0.2	0.2
Total	100	100	100	100	100	100	100	100	100	100	100	100	100	100	100	100	100	100	100	100	100
LOI	1.24	1.26	2.81	2.1	2.38	2.55	2.24	1.96	1.36	1.49	1.61	2.62	2.92	7.33	6.56	5.4	7.3	1.94	4.86	4.23	5.92
AR	2.48	2.49	1.9	2.07	2.06	2.24	2.29	2.24	2.59	2.67	2.7	2.43	2.43	1.01	1.01	1.01	1.04	1.23	1.61	1.44	1.05
σ	0.98	0.86	1.03	0.77	0.99	2.19	1.65	1.21													
Na_2O+K_2O/Al_2O_3	0.448	0.449	0.316	0.357	0.355	0.404	0.42	0.408	0.478	0.488	0.49	0.446	0.44	0.004	0.003	0.004	0.019	0.188	0.348	0.271	0.024
SI	5.15	5.15	8.49	7.14	7.26	19.14	17.62	17.7	10.99	10.72	10.65	22.57	23.02	30.8	32	25.57	31.69	29.14	21.77	34.58	23.99
Na_2O+K_2O	5.85	5.56	5.44	5.07	5.55	6.89	6.49	5.84	7.29	7.83	7.73	7.8	7.7	0.05	0.04	0.05	0.3	1.81	4.59	4.14	0.3
$Mg^{\#}$	31.18	30.71	31.42	30.03	31.03	49.48	48.77	49.02	43.21	45.46	44.76	54.88	54.62	47.16	48.53	40.77	48.39	46.94	41.78	58.09	38.91
A/CNK	1.47	1.43	2.67	2.3	2.33	1.61	1.47	1.53	1.19	1.2	1.21	1.34	1.38	38.47	34.29	29.37	34.83	0.54	0.71	0.77	17.22
A/NK	1.72	1.66	2.89	2.56	2.58	1.91	1.82	1.88	1.45	1.42	1.42	1.6	1.61	175.59	223.44	176.45	47.81	3.37	1.91	2.69	38.54
Ba	829	655	816	493	546	998	884	889	967	988	969	920	822	5.8	2.1	12.5	24.4	46.7	396	309	58
Rb	210	183.5	352	366	419	152.5	159.5	148.5	107	113.5	115.5	125.5	112.5	1.5	0.9	8.6	71.1	14.1	84.3	315	35.1
Sr	186.5	169	50	17.8	21.4	157.5	184	167.5	385	392	371	307	259	12.6	4.6	3.5	3.7	93.9	230	168.5	1.8
Zr	155	148	310	218	272	157	159	146	150	159	145	181	199	72	64	63	31	55	62	39	65
Nb	11.9	11	20.1	11.2	13.7	8.3	6.9	6.1	7.7	7.5	7.4	7.3	7.8	3.2	2.7	3.2	1.3	5.7	3.4	2	2.8
Ni																24.4	96.6	131	52.9	141	51.6

(Continued)

Table 4. (*Continued*)

Co																53.2	42	32.9	32.8	37.4	32.6
Zn																148	108	107	89	78	175
Cr	60	60	40	30	30	150	110	110	70	70	70	180	190	120	130	10	110	360	150	790	60
La	28.1	27.1	24.7	15.2	22.3	37.1	38.1	28.2	33	33.9	33.3	34	32.8	12.4	10.8	4.4	1.7	2.1	8.7	2.2	6.7
Ce	58.4	54.9	67.4	38.8	42	72.1	71.7	53.5	61.7	64.2	65.7	63	61.1	25.4	23.3	10.9	5	6.3	17.7	6.1	13.6
Pr	5.99	5.59	6.04	3.65	5.17	8.26	8.13	6.12	6.7	6.81	6.77	7.38	7.1	3.66	3.4	1.51	0.8	0.99	1.99	0.96	1.53
Nd	20.7	19.7	21.9	13.2	17.8	30	29.3	22.4	24.1	24.7	24.1	26.1	25.4	17.6	16.4	7.6	4	4.9	8.6	4.8	6
Sm	3.78	3.52	4.07	2.62	3.34	5.06	4.92	3.78	4.24	4.34	4.2	4.35	4.21	5.21	5.05	2.45	1.46	1.48	2.26	1.61	1.81
Eu	0.61	0.58	0.73	0.43	0.56	1.15	1.24	0.97	1.2	1.17	1.15	1	0.95	1.48	1.52	0.73	0.75	0.63	0.78	0.53	0.5
Gd	3.12	2.97	3.54	2.6	2.92	3.85	3.64	2.88	3.62	3.54	3.49	3.44	3.24	6.56	6.89	3.24	1.88	1.99	2.89	2.24	3.46
Tb	0.5	0.48	0.59	0.42	0.47	0.54	0.51	0.39	0.5	0.5	0.49	0.48	0.46	1.04	1.11	0.55	0.37	0.35	0.47	0.42	0.81
Dy	3.01	2.83	3.49	2.54	2.84	3.03	2.76	2.24	2.84	2.76	2.7	2.71	2.77	6.77	7.21	3.8	2.45	2.42	3.11	2.71	6.46
Ho	0.61	0.59	0.71	0.52	0.56	0.56	0.53	0.43	0.56	0.55	0.53	0.54	0.55	1.41	1.47	0.8	0.55	0.53	0.68	0.6	1.66
Er	1.81	1.84	2.27	1.56	1.84	1.68	1.56	1.23	1.64	1.62	1.53	1.58	1.66	4.26	4.21	2.35	1.69	1.57	1.96	1.75	5.53
Tm	0.3	0.29	0.37	0.26	0.31	0.25	0.23	0.19	0.25	0.25	0.24	0.24	0.25	0.62	0.62	0.37	0.28	0.25	0.3	0.26	0.92
Yb	1.92	1.87	2.43	1.66	2.13	1.65	1.49	1.24	1.52	1.46	1.44	1.52	1.58	3.58	3.69	2.46	1.94	1.68	1.92	1.71	6.26
Lu	0.31	0.3	0.39	0.26	0.35	0.27	0.24	0.2	0.25	0.25	0.25	0.25	0.27	0.59	0.62	0.39	0.29	0.25	0.29	0.26	0.99
REE	129.16	122.56	138.63	83.72	102.59	165.5	164.35	123.77	142.12	146.05	145.89	146.59	142.34	90.58	86.29	41.55	23.16	25.44	51.65	26.15	56.23
LREE	117.58	111.39	124.84	73.9	91.17	153.67	153.39	114.97	130.94	135.12	135.22	135.83	131.56	65.75	60.47	27.59	13.71	16.4	40.03	16.2	30.14
HREE	11.58	11.17	13.79	9.82	11.42	11.83	10.96	8.8	11.18	10.93	10.67	10.76	10.78	24.83	25.82	13.96	9.45	9.04	11.62	9.95	26.09
LREE/HREE	10.15	9.97	9.05	7.53	7.98	12.99	14	13.06	11.71	12.36	12.67	12.62	12.2	2.65	2.34	1.98	1.45	1.81	3.44	1.63	1.16
Eu/Eu*	0.54	0.55	0.59	0.5	0.55	0.8	0.9	0.9	0.94	0.91	0.92	0.79	0.79	0.77	0.79	0.79	1.38	1.12	0.93	0.85	0.61
Ce/Ce*	1.03	1.02	1.29	1.22	0.91	0.95	0.94	0.94						0.9	0.92	1.02	1.03	1.05	0.99	1.01	0.99
$(La/Yb)_N$	9.87	9.77	6.85	6.17	7.06	15.16	17.24	15.33	14.64	15.65	15.59	15.08	14	2.34	1.97	1.21	0.59	0.84	3.05	0.87	0.72
$(La/Sm)_N$	4.68	4.84	3.82	3.65	4.2	4.61	4.87	4.69	4.9	4.91	4.99	4.92	4.9	1.5	1.35	1.13	0.73	0.89	2.42	0.86	2.33
$(Ce/Yb)_N$	7.87	7.59	7.17	6.05	5.1	11.3	12.45	11.16	10.5	11.37	11.8	10.72	10	1.84	1.63	1.15	0.33	0.48	2.38	0.46	0.56
$(Ce/Sm)_N$	3.73	3.76	4	3.57	3.03	3.44	3.52	3.42	3.51	3.57	3.78	3.5	3.5	1.18	1.11	1.07	0.41	0.51	1.89	0.46	1.81
$(Eu/Yb)_N$	0.9	0.88	0.85	0.74	0.75	1.98	2.37	2.22	2.24	2.28	2.27	1.87	1.71	1.18	1.17	0.84	1.1	1.07	1.16	0.88	0.23
Y	18.4	18	20.2	14.5	16.6	15.2	14	11.3	16.4	15.1	14.8	15.4	15.6	38	39.1	20.7	13	14.6	18.7	16.3	44.6
Cs	6.31	5.31	12.65	12	12.9	2.44	3.49	2.83	4.41	3.08	3.08	23.3	19.8	0.68	0.52	1.4	3.75	0.93	0.87	18.2	9.03
Ta	1.2	1.1	1.4	0.8	0.9	0.6	0.5	0.4	0.6	0.6	0.6	0.6	0.6	0.2	0.2	0.2	0.1	0.6	0.3	0.1	0.2
Hf	4.8	4.4	7.8	5.8	6.9	4.2	4.2	3.6	3.9	4	4	4.8	5.2	2	1.8	2.1	0.9	1.8	1.9	1.2	1.9
Th	21.7	20.2	23.9	15	18.45	11.4	10.85	9.1	13.55	12.95	13.2	12.1	13	0.57	0.51	0.56	0.23	3	2.65	0.36	3.32
U	3.75	3.84	7.74	6.14	7.06	2.68	2.58	2.16	2.92	2.6	2.63	2.26	2.28	0.28	0.21	0.3	0.51	0.91	0.62	0.08	0.93
V																444	223	160	211	149	508

Table 5. Geochemical parameters (all in ppm) of the Anshan Group meta-sandstones versus tectonic setting (after (Bhatia, 1983; Bhatia and Crook, 1986))

Tectonic environment	Oceanic island arcs	Continental island arcs	Active continental margins	Passive continental margins	Meta-sandstones of the Anshan Group
La	8 ± 1.7	27 ± 4.5	37	39	32.8~33
Ce	19 ± 3.7	59 ± 8.2	78	85	61.1~65.7
ΣREE	58 ± 10	146 ± 20	186	210	142.12~146.05
LREE/HREE	3.8 ± 0.9	7.7 ± 1.7	9.1	8.5	11.71~12.67
La/Yb	4.2 ± 1.3	11.0 ± 3.6	12.5	15.9	20.76~23.22
$(La/Yb)_N$	2.8 ± 0.9	7.5 ± 2.5	8.5	10.5	14.00~15.65
δEu	1.04 ± 0.11	0.79 ± 0.13	0.6	0.56	0.79~0.94
Rb/Sr	0.05 ± 0.05	0.65 ± 0.33	0.89 ± 0.24	1.19 ± 0.40	0.28~0.43
Zr/Th	48.0 ± 13.4	21.5 ± 2.4	9.5 ± 0.7	19.1 ± 5.8	10.98~15.31
La/Sc	0.55 ± 0.22	1.82 ± 0.3	4.55 ± 0.8	6.25 ± 1.4	
La/Y	0.48 ± 0.12	1.02 ± 0.07	1.33 ± 0.09	1.31 ± 0.26	2.01~2.25
La/Th	4.26 ± 1.20	2.36 ± 0.30	1.77 ± 1.1	2.20 ± 0.47	2.44~2.81
Zr/Hf	46	36	26	30	36.25~39.75
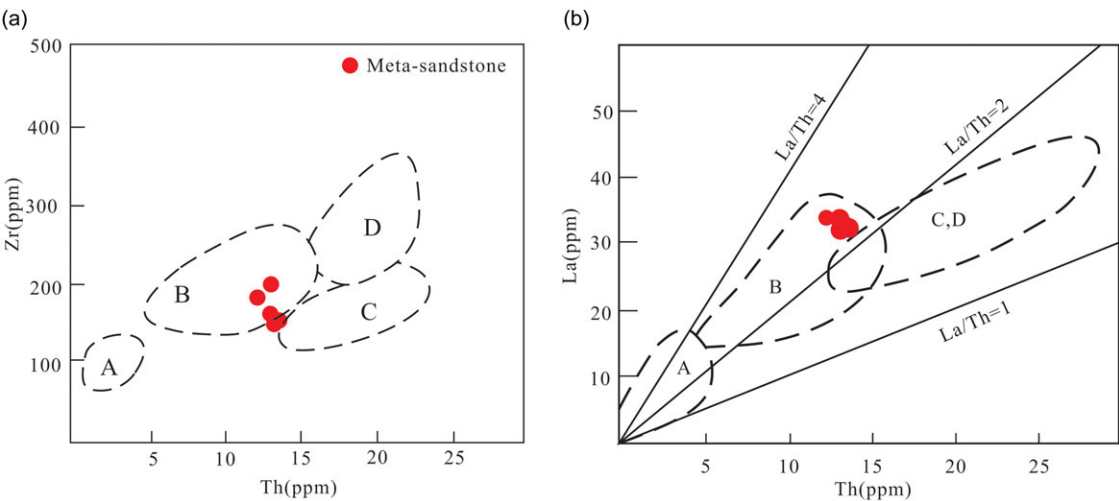
Figure 13. Tectonic setting discrimination diagrams of meta-sandstones. (a) after Pearce J A, 1973; (b) after M. R. Bhatia, 1988; A, oceanic island arc; B, continental island arc; C, active continental margin; D, passive continental margin.

References

Agrawal S, Guevara M, Verma SP (2008) Tectonic Discrimination of Basic and Ultrabasic Volcanic Rocks through Log-Transformed Ratios of Immobile Trace Elements. *International Geology Review* **50**, 1057–1079.

Andersen T (2002) Correction of common lead in U–Pb analyses that do not report [204]Pb. *Chemical Geology* **192**, 59–79.

Bai X, Liu S, Yan M, Zhang L, Wang W, Guo R and Guo B (2014) Geological event series of Early Precambrian metamorphic complex in South Fushun area, Liaoning Province. *Acta Petrologica Sinica* **30**(10): 2905–2924.

Balakrishnan S, Hanson GN, Rajamani V (1991) Pb and Nd isotope constraints on the origin of high Mg and tholeiitic amphibolites, Kolar Schist Belt, South India. *Contributions to Mineralogy and Petrology* **107**, 279–92.

Bao H, Liu S, Wang M, Teng G, Sun G (2020) Mesoarchean geodynamic regime evidenced from diverse granitoid rocks in the Anshan-Benxi area of the North China Craton. *Lithos* **366–367**.

Bas MJL, Maitre RWL, Streckeisen A, Zanettin B (1986) A Chemical Classification of Volcanic Rocks Based on the Total Alkali-Silica Diagram. *Journal of Petrology* **27**, 745–750.

Beard JS, Lofgren GE (1991) Dehydration Melting and Water-Saturated Melting of Basaltic and Andesitic Greenstones and Amphibolites at 1, 3, and 6. 9 kb. *Journal of Petrology* **32**, 365–401.

Bhatia MR (1983) Plate tectonics and geochemical composition of sandstones. *The Journal of Geology* **91**, 611–27.

Bhatia MR, Crook KAW (1986) Trace element characteristics of graywackes and tectonic setting discrimination of sedimentary basins. *Contributions to Mineralogy and Petrology* **92**, 181–93.

Boynton WV (1984) Chapter 3 - Cosmochemistry of the Rare Earth Elements: Meteorite Studies, In: *Developments in Geochemistry* (ed Henderson, P., pp. 63–114. Elsevier.

Dai Y, Zhang L, Wang C, Liu L, Cui M, Zhu M and Xiang P (2012) Genetic type, formation age, and tectonic setting of the Waitoushan banded iron formation, Benxi, Liaoning, Province. *Acta Petrologica Sinica* **28** (11): 3574–3594.

Dai Y, Zhang L, Zhu M, Wang C, Liu L (2013a) Archean BIF mineralization, crustal accretion, and ore-rich genesis in Anshan-Benxi area. *Mineralogy* **33**, 386–387.

Dai Y, Zhang L, Zhu M, Wang C and Liu L (2013b) Chentaigou BIF-type iron deposit, Anshan area associated with Archean crustal growth: Constraints from zircon U-Pb dating and Hf isotope. *Acta Petrologica Sinica* **29**(7): 2537–2550.

Eggins SM, Kinsley LPJ, Shelley JMG (1998) Deposition and element fractionation processes during atmospheric pressure laser sampling for analysis by ICP-MS. *Applied Surface Science* **127-129**, 278–86.

Geng Y, Shen Q and Ren L (2010) Late Neoarchean to Early Paleoproterozoic magmatic events and tectonothermal systems in the North China Craton. *Acta Petrologica Sinica* **26**(7):1945–66.

Geng YS, Liu FL, Yang CH (2006) Magmatic event at the end of the Archean in eastern Hebei Province and its geological implication. *Acta Geologica Sinica-English Edition* **80**, 819–33.

Green TH (1994) Experimental studies of trace-element partitioning applicable to igneous petrogenesis — Sedona 16 years later. *Chemical Geology* **117**, 1–36.

Gromet LP, Haskin LA, Korotev RL, Dymek RF (1984) The "North American shale composite": Its compilation, major and trace element characteristics. *Geochimica et Cosmochimica Acta* **48**, 2469–2482.

Guo H (1994) The tectonic evolution sequence of Archean crust in Anshan area. Regional Geology of China, 1-9.

Guo R, Li Z, Liu S, Wang M, Bao H, Wang W, Huang X, Dou Y (2022) Late Neoarchean geodynamic regime of the northeastern North China Craton: constraints from metamorphosed volcanic rocks of the Anshan-Benxi greenstone belt. *Precambrian Research* **371**, 106583.

Guo R, Liu S, Gong E, Wang W, Wang M, Fu J, Qin T (2017) Arc-Generated metavolcanic rocks in the Anshan–Benxi greenstone belt, North China Craton: Constraints from geochemistry and zircon U–Pb–Hf isotopic systematics. *Precambrian Research* **303**, 228–250.

Harris N, Pearce J, Tindle A (1986) Geochemical characteristics of collision zone magmatism. *Geological Society London Special Publications* **19**, 67–81.

Hollings P, Kerrich R (1999) Trace element systematics of ultramafic and mafic volcanic rocks from the 3 Ga North Caribou greenstone belt, northwestern Superior Province. *Precambrian Research* **93**, 257–79.

Hollings P, Wyman D, Kerrich R (1999) Komatiite–basalt–rhyolite volcanic associations in Northern Superior Province greenstone belts: significance of plume-arc interaction in the generation of the proto continental Superior Province. *Lithos* **46**, 137–61.

Hu Z, Zhang W, Liu Y, Gao S, Li M, Zong K, Chen H, Hu S (2015) "Wave" Signal-Smoothing and Mercury-Removing Device for Laser Ablation Quadrupole and Multiple Collector ICPMS Analysis: Application to Lead Isotope Analysis. *Analytical Chemistry* **87**, 1152–1157.

Huang B, Kusky TM, Johnson TE, Wilde SA, Wang L, Polat A, Fu D (2020) Paired metamorphism in the Neoarchean: A record of accretionary-to-collisional orogenesis in the North China Craton. *Earth and Planetary Science Letters* **543**, 116355.

Jackson SE, Pearson NJ, Griffin WL, Belousova EA (2004) The application of laser ablation-inductively coupled plasma-mass spectrometry to in situ U–Pb zircon geochronology. *Chemical Geology* **211**, 47–69.

Kerrich R, Polat A, Xie Q (2008) Geochemical systematics of 2.7 Ga Kinojevis Group (Abitibi), and Manitouwadge and Winston Lake (Wawa) Fe-rich basalt–rhyolite associations: Backarc rift oceanic crust? *Lithos* **101**, 1–23.

Khoza D, Jones AG, Muller MR, Evans RL, Webb SJ, Miensopust M (2013) Tectonic model of the Limpopo belt: Constraints from magnetotelluric data. *Precambrian Research* **226**, 143–56.

Kröner A, Wilde SA, Li JH, Wang KY (2005) Age and evolution of a late Archean to Paleoproterozoic upper to lower crustal section in the Wutaishan/Hengshan/Fuping terrain of northern China. *Journal of Asian Earth Sciences* **24**, 577–95.

Kusky TM (2011) Geophysical and geological tests of tectonic models of the North China Craton. *Gondwana Research* **20**, 26–35.

Li J, Qian X (1995) Structural characteristics of the Hengshan greenstone belt -Evidence of Late Archean continental rifting. North China Journal of Geology and Mineral Resources, 181–189.

Li L, Zhang L, Dai Y, Wang C, Li Z (2012) Formation age,geochemical signatures and geological significance of the Sanheming BIF-type iron deposit in the Guyang greenstone belt, Inner Mongolia. *Acta Petrologica Sinica* **28**, 3623–3637.

Li P, Guo W, Guan Q and Liu J (2016) Late Neoarchean crustal growth in the northeast of the North China Craton: Evidence from the geochronology and Hf isotope composition of Banshigou supracrustal rocks. *Acta Petrologica Sinica* **32** (9): 2839–2855.

Lian G, Ren Y, Shi J, Xu Z, Feng F (2023) Petrogenesis of the ~1.94 Ga Meta-gabbronorites in Liangcheng: Implications for Tectonic Evolution of the Khondalite Belt, North China Craton. *Acta Geologica Sinica - English Edition* **97**, 418–435.

Liu J-m, Zhao Y, Sun Y-l, Li D-p, Liu J, Chen B-l, Zhang S-h, Sun W-d (2010) Recognition of the latest Permian to Early Triassic Cu–Mo mineralization on the northern margin of the North China block and its geological significance. *Gondwana Research* **17**, 125–34.

Liu L, Zhang L, Dai Y, Wang C and Li Z (2012) Formation age, geochemical signatures, and geological significance of the Sanheming BIF-type iron deposit in the Guyang greenstone belt, Inner Mongolia. *Acta Petrologica Sinica* **28**(11), 3623–37.

Liu X, Li J, Liu Y, Li W, Wen Q, Liang C and Chang R (2017) Kinematics Analysis and Formation Mechanism of Qidashan Ductile Shear Zone, Eastern Anshan, Liaoning Province, NE China. Earth *Science* **42**, 2129–45.

Manikyamba C (2004) Geochemical systematics of tholeiitic basalts from the 2.7 Ga Ramagiri-Hungund composite greenstone belt, Dharwar craton. *Precambrian Research* **134**, 21–39.

Manikyamba C, Kerrich R, Khanna TC, Keshav Krishna A, Satyanarayanan M (2008) Geochemical systematics of komatiite–tholeiite and adakitic-arc basalt associations: The role of a mantle plume and convergent margin in formation of the Sandur Superterrane, Dharwar craton, India. *Lithos* **106**, 155–72.

Mckibben MA, Shanks WC, Ridley WI (1998) Applications of Microanalytical Techniques to Understanding Mineralizing Processes.

McLennan SM (1989) Rare earth elements in sedimentary rocks; influence of provenance and sedimentary processes. *Reviews in Mineralogy and Geochemistry* **21**, 169–200.

McLennan SM, Taylor SR (1991) Sedimentary rocks and crustal evolution: tectonic setting and secular trends. *The Journal of Geology* **99**, 1–21.

Meschede M (1986) A method of discriminating between different types of mid-ocean ridge basalts and continental tholeiites with the Nb 1bZr 1bY diagram. *Chemical Geology* **56**, 207–218.

Miyashiro A (1974) Volcanic rock series in island arcs and active continental margins. *American Journal of Science* **274**, 321–355.

Mullen ED (1983) MnO/TiO2/P2O5: a minor element discriminant for basaltic rocks of oceanic environments and its implications for petrogenesis. *Earth and Planetary Science Letters* **62**, 53–62.

Pearce J (1982) Trace Element Characteristics of Lavas from Destructive Plate Boundaries, 525–548.

Pearce J, Harris N, Tindle A (1984) Trace Element Discrimination Diagrams for the Tectonic Interpretation of Granitic Rocks. *Journal of Petrology* **25**, 956–983.

Polat A, Hofmann AW (2003) Alteration and geochemical patterns in the 3.7–3.8 Ga Isua greenstone belt, West Greenland. *Precambrian Research* **126**, 197–218.

Polat A, Kerrich R, Wyman DA (1999) Geochemical diversity in oceanic komatiites and basalts from the Late Archean Wawa greenstone belts, Superior Province, Canada: trace element and Nd isotope evidence for a heterogeneous mantle. *Precambrian Research* **94**, 139–73.

Prendergast MD (2004) The Bulawayan Supergroup: a late Archaean passive margin-related large igneous province in the Zimbabwe craton. *Journal of the Geological Society* **161**, 431–45.

Ross P-S, Bédard JHBH (2009) Magmatic affinity of modern and ancient subalkaline volcanic rocks determined from trace element discriminant diagrams. *Canadian Journal of Earth Sciences* **46**, 823–839.

Said N, Kerrich R, Groves D (2010) Geochemical systematics of basalts of the lower basalt unit, 2.7Ga Kambalda sequence, Yilgarn craton, Australia: Plume impingement at a rifted craton margin. *Lithos* **115**, 82–100.

Shand SJ (1943) The eruptive rocks: 2nd edition, New York: John Wiley, p. 444.

Song B, Nutman AP, Liu D, Wu J (1996) 3800 to 2500 Ma crustal evolution in the Anshan area of Liaoning Province, northeastern China. *Precambrian Research* **78**, 79–94.

Song B, Wu J, Wan Y and Liu D (1994) The age of Chentaigou metamorphic supracrustal rocks in the Anshan area. *Liaoning Geology*, 12–15.

Song B, Zhang Y, Wan Y, Jian P (2002) Zircon SHRIMP sample target preparation, age determination, and related phenomenon discussion. *Geological Review* **48**, 26–30.

Stiegler MT, Lowe DR, Byerly GR (2008) Abundant pyroclastic komatiitic volcanism in the 3.5–3.2 Ga Barberton greenstone belt, South Africa. *Geology* **36**, 779–82.

Stolz AJ, Jochum KP, Spettel B, Hofmann AW (1996) Fluid- and melt-related enrichment in the subarc mantle: Evidence from Nb/Ta variations in island-arc basalts. *Geology* **24**, 587–90.

Sun S-s, McDonough WF (1989) Chemical and isotopic systematics of oceanic basalts: implications for mantle composition and processes. *Geological Society, London, Special Publications* **42**, 313–45.

Tarney J (1976) Geochemistry of Archean high grade gneisses with implications as to origin and evolution of the Precambrian crust. In: *The Early History of Earth* (ed. Windley, B.F.), pp. 405–17. Wiley, London.

Taylor SR, McLennan SM, (1985) The continental crust : its composition and evolution : an examination of the geochemical record preserved in sedimentary rocks.

Tong X, Wang C, Peng Z, Huang H, Zhang L, Zhai M (2019) Geochemistry of meta-sedimentary rocks associated with the Neoarchean Dagushan BIF in the Anshan-Benxi area, North China Craton: Implications for their provenance and tectonic setting. *Precambrian Research* **325**, 172–91.

Vermeesch P (2018) IsoplotR: A free and open toolbox for geochronology. *Geoscience Frontiers* **9**, 1479–93.

Walker KR, Joplin GA, Lovering JF, Green R (1959) Metamorphic and metasomatic convergence of basic igneous rocks and lime-magnesia sediments of the precambrian of North-western Queensland. *Journal of the Geological Society of Australia* **6**, 149–77.

Wan Y (1992) Formation and evolution of iron-bearing rock series in Gongchangling, Liaoning.

Wan Y, Li R, Wilde SA, Liu D, Chen Z, Yan L, Song T, Yin X (2005) UHP metamorphism and exhumation of the Dabie Orogen, China: Evidence from SHRIMP dating of zircon and monazite from a UHP granitic gneiss cobble from the Hefei Basin. *Geochimica et Cosmochimica Acta* **69**, 4333–48.

Wan Y, Liu D, Wang S, Dong C, Yang E, Wang W, Zhou H, Ning Z, Du L, Yin X (2010) Juvenile magmatism and crustal recycling at the end of the Neoarchean in Western Shandong Province, North China Craton: Evidence from SHRIMP zircon dating. *American Journal of Science* **310**, 1503–52.

Wan Y, Liu D, Yin X, Wilde SA, Xie L, Yang Y, Zhou H, Wu J (2007) SHRIMP geochronology and Hf isotope composition of zircons from the Tiejiashan granite and supracrustal rocks in the Anshan area, Liaoning province. *Acta Petrologica Sinica* **23**, 241–252.

Wan Y, Song B, Yang C, Liu D (2005) SHRIMP zircon U-Pb geochronology and its geological significance of Archean rocks in Fushun-Qingyuan area, Liaoning Province. *Geological Journal*, 78–87.

Wan Y, Song Z, Wang L, Xie H, Liu S, Hou J, Dong C, Xie S, Bai W, Liu D (2017) Early Precambrian evolution of the Qixia area, eastern North China Craton: Evidence from geological mapping and SHRIMP U-Pb zircon dating. *Geological Bulletin of China* **36**(11), 1927–41.

Wang C, Huang H, Tong X, Zheng M, Peng Z, Nan J, Zhang L, Zhai M (2016) Changing provenance of late Neoarchean metasedimentary rocks in the Anshan-Benxi area, North China Craton: Implications for the tectonic setting of the world-class Dataigou banded iron formation. *Gondwana Research* **40**, 107-123.

Wang C, Peng Z, Tong X, Huang H, Zheng M, Zhang L, Zhai M (2018) Late Neoarchean supracrustal rocks from the Anshan-Benxi terrane, North China Craton: New geodynamic implications from the geochemical record. *American Journal of Science* **317**, 1095–1148.

Wang E, Xia J, Zhao F, Fu J, Hou G (2013) Material sources and sedimentary environment of Gongchangling iron deposit. *Mineral Deposits* **32**, 380–396.

Wang W (2010) The Formation and Evolution of granite-greenstone belt in the Qixingtai area, Western Shandong Province: constraints of geology, SHRIMP dating, and geochemistry.

Winchester JA, Floyd PA (1977) Geochemical discrimination of different magma series and their differentiation products using immobile elements. *Chemical Geology* **20**, 325–43.

Wood DA (1980) The application of a ThHfTa diagram to problems of tectonomagmatic classification and to establishing the nature of crustal contamination of basaltic lavas of the British Tertiary Volcanic Province. *Earth and Planetary Science Letters* **50**, 11–30.

Wright JB (1969) A simple alkalinity ratio and its application to questions of non-orogenic granite genesis. *Geological Magazine* **106**, 370–384.

Wu M, Lin S, Wan Y, Gao J-F, Stern RA (2021) Episodic Archean crustal accretion in the North China Craton: Insights from integrated zircon U-Pb-Hf-O isotopes of the Southern Jilin Complex, northeast China. *Precambrian Research* **358**, 106150.

Wyman D, Kerrich R (2009) Plume and arc magmatism in the Abitibi subprovince: Implications for the origin of Archean continental lithospheric mantle. *Precambrian Research* **168**, 4–22.

Wyman DA (1999) A 2.7 Ga depleted tholeiite suite: evidence of plume-arc interaction in the Abitibi Greenstone Belt, Canada. *Precambrian Research* **97**, 27–42.

Wyman DA, Kerrich R, Polat A (2002) Assembly of Archean cratonic mantle lithosphere and crust: plume–arc interaction in the Abitibi–Wawa subduction–accretion complex. *Precambrian Research* **115**, 37–62.

Xiang P, Cui M, Wu H, Zhang X and Zhang L (2012) Geological characteristics, ages of host rocks, and the geological significance of the Zhoutaizi iron deposit in Luanping, Hebei Province. *Acta Petrologica Sinica*, **28**(11), 3655–69.

Yang J, Wang J, Zhang Q, Chen W, Pan Z, Du X, Jiao S and Wang S (2016) Global IAB data excavation: The performance in basalt discrimination diagrams and preliminary interpretation. *Geological Bulletin of China* **35**(12),1937–49.

Yang X (2013) Study on iron Ore-Forming process of metamorphic terrainin Anshan-Benxi area, Liaoning province, China.

Yin X (2006) Geochronology and Geochemistry of the Tiejiashan granites andsupercrustal rocks in the Anshan area, Liaoning Province.

Yu C, Yang T, Zhang J, Zhao G, Cawood PA, Yin C, Qian J, Gao P, Zhao C (2022) Coexisting diverse P–T–t paths during Neoarchean Sagduction: Insights from numerical modeling and applications to the eastern North China Craton. *Earth and Planetary Science Letters* **586**, 117529.

Yuan, H, Gao, S., Liu, X., Li, H., Günther, D., Wu, F.-Y., (2004) Accurate U-Pb Age and trace element determinations of zircon by laser ablation-inductively coupled plasma-mass spectrometry. *Geostandards and Geoanalytical Research* **28**, 353–370.

Zhai M (2010) Tectonic evolution and metallogenesis of North China Craton. *Mineral Deposits* **29**, 24–36.

Zhai M (2012) Evolution of the North China Craton and Early Plate Tectonics. *Acta Geologica Sinica* **86**, 1335–1349.

Zhang C, Shi S, Shi Y (2021) Tectonic evolution of Northern Margin of Eastern North China Craton: evidences of Middle Triassic Plutons in Faku Area, Liaoning Province. *Journal of Jilin University (Earth Science Edition)* **51**(3), 734–48.

Zhang J, Jin W, Zheng P, Wang Y, Li B, Cai L, Wang Q (2013) Identification and zircon U-Pb geochronology of the Yingchengzi Paleoarchean gneiss complex, Anshan area. *Acta Petrologica Sinica* **29**, 399-413.

Zhang W, Hu Z, Spectroscopy A (2020) Estimation of Isotopic Reference Values for Pure Materials and Geological Reference Materials[J]. *Atomic Spectroscopy* **41**(3), 93–102.

Zhang X, Zhang L, Xiang P, Wan B, Pirajno F (2011) Zircon U–Pb age, Hf isotopes and geochemistry of Shuichang Algoma-type banded iron-formation, North China Craton: constraints on the ore-forming age and tectonic setting. *Gondwana Research* **20**, 137–48.

Zhang Z, Hu B, Zhang D, Xiong G, Zhu X, Jia W, Gong X (2020) Zircon U–Pb age, geochemistry and Hf isotope characteristics of Shimensi granite porphyry in northern Jiangxi Province and its constraint on mineralization. *Geological Bulletin of China* **39**(8), 1267–84.

Zhao G, Cawood PA, Wilde SA, Sun M, Lu L (2000) Metamorphism of basement rocks in the Central Zone of the North China Craton: implications for Paleoproterozoic tectonic evolution. *Precambrian Research* **103**, 55–88.

Zhao G, Sun M, Wilde SA (2002) Characteristics of basement tectonic units of North China Craton and Early Proterozoic assembly. *Scientia Sinica(Terrae)*, 538–549.

Zhao G, Sun M, Wilde SA, Sanzhong L (2005) Late Archean to Paleoproterozoic evolution of the North China Craton: key issues revisited. *Precambrian Research* **136**, 177–202.

Zhao G, Zhai M (2013) Lithotectonic elements of Precambrian basement in the North China Craton: Review and tectonic implications. *Gondwana Research* **23**, 1207–40.

Zhou H, Liu D, Wan Y, Dong C (2008) 3.3-3.1 Ga magmatism in the Dongshan complex, Anshan area, Liaoning, China: Evidence from zircon SHRIMP U-Pb dating. *Geological Bulletin of China* **27**, 2122–2126.

Zhu K (2016) The formation and evolution of the Archean greenstone belt in the Anshan-Benxi area.

Zhu K, Liu Z, Xu Z, Wang X (2016) Chronology, petro-geochemistry and genesis of Donganshan granite in Anshan area. *Acta Petrologica Sinica* **32**, 590–604.

Zhu M, Dai Y, Zhang L, Wang C, Liu L (2015) Geochronology and geochemistry of the Nanfen iron deposit in the Anshan-Benxi area, North China Craton: implications for ~2.55Ga crustal growth and the genesis of high-grade iron ores. *Precambrian Research* **260**, 23–38.